Endosomes deliver ceramide phosphoethanolamine with unique acyl chain anchors to the cleavage furrow during male meiotic cytokinesis

Govind Kunduri[1*], Si-Hung Le [2], Valentina Baena[3&4], Nagampalli Vijaykrishna[5], Adam Harned[3&4], Kunio Nagashima[3&4], Daniel Blankenberg[5], Yoshihiro, Izumi[2], Kedar Narayan[3&4], Takeshi Bamba[2], Usha Acharya[1*] and Jairaj K.Acharya[1]*.

1. Cancer and Developmental Biology Laboratory, National Cancer Institute, Frederick, MD 21702.
2. Division of Metabolomics, Medical Institute of Bioregulation, Kyushu University, Fukuoka 812-8582, Japan.
3. Center for Molecular Microscopy, Center for Cancer Research, National Cancer Institute, National Institutes of Health, Bethesda 20892, Maryland, USA.
4. Cancer Research Technology Program, Frederick National Laboratory for Cancer Research, Frederick 21702, Maryland, USA.
5. Genomic Medicine Institute and Lerner Research Institute, Cleveland Clinic, Cleveland, OH.

* Corresponding authors: kunduri.govind@nih.gov; usha.acharya@nih.gov ; acharyaj@mail.nih.gov

Abstract

Cell division, wherein one cell divides into two daughter cells, is fundamental to all living organisms. Cytokinesis, the final step in cell division, begins with the formation of an actomyosin contractile ring, positioned midway between the segregated chromosomes. Constriction of the ring with concomitant membrane deposition in a spatiotemporal manner generates a cleavage furrow that physically separates the cytoplasm. Unique lipids with specific biophysical properties have been shown to localize to intercellular bridges (also called midbody) connecting the two dividing cells; however, their biological roles and delivery mechanisms remain largely unknown. In this study, we show that Ceramide phosphoethanolamine (CPE), the structural analog of sphingomyelin, has unique acyl chain anchors in spermatocytes and is essential for meiotic cytokinesis. The head group of CPE is also important for spermatogenesis. We find that aberrant central spindle and contractile ring behavior but not mislocalization of phosphatidylinositol phosphates (PIPs) at the plasma membrane is responsible for the male meiotic cytokinesis defect in CPE deficient animals. Further, we demonstrate the enrichment of CPE in multivesicular bodies marked by Rab7, which in turn localize to cleavage furrow. Volume electron microscopy analysis using correlative light and focused ion beam scanning electron microscopy shows that CPE enriched Rab7 positive endosomes are juxtaposed on contractile ring material. Correlative light and transmission electron microscopy reveal Rab7 positive endosomes as a multivesicular body-like organelle that releases its intraluminal vesicles in the vicinity of ingressing furrows. Genetic ablation of Rab7 or expression of dominant negative Rab11 results in significant meiotic cytokinesis defects. Our results imply that endosomal delivery of CPE to ingressing membranes is crucial for meiotic cytokinesis.

45 ## Introduction

46 Eukaryotic cells display high diversity in lipid species that are chemically and structurally distinct.
47 They are classified into eight major categories, each of which is further subdivided into classes
48 and subclasses [1]. Lipids usually comprise of a polar head group that is linked by a structural
49 backbone to hydrophobic tail groups composed of acyl chains. Lipid diversity that exists in cells
50 arises from the large number of combinatorial chemical possibilities that the head and tail moieties
51 can generate. Diversification of lipids to cope with evolving cellular complexity has resulted in
52 thousands of lipid species with purported unique functions, most of which still remain unknown
53 [2].

54 The head groups of each lipid class have been widely recognized for their biological function. For
55 instance, the inositol head group of phosphatidylinositol phosphates (PIPs) and its modifications
56 play critical roles in cellular signaling [3]. However, even within each lipid class, there are a
57 number of molecularly distinct species that have identical head group but differ extensively in their
58 acyl side chains, such as number of carbon atoms, number of double bonds, and the nature of the
59 chemical linkage (e.g., ester or ether). An increasing number of studies are beginning to reveal the
60 importance of acyl side chains by demonstrating that they selectively bind to target proteins and
61 elicit biological function [4, 5]. For instance, a recent study showed that the acyl side chains of
62 diacylglycerol significantly influence the recruitment of protein kinase C to the plasma membrane
63 [6]. Similarly, ceramide chain length was shown to be critical for selective protein cargo sorting
64 at endoplasmic reticulum (ER) exit sites in yeast [7]. The COPI machinery protein p24 bound
65 specifically to N-stearoyl sphingomyelin (SM C18) and functioned as a cofactor to regulate COPI-
66 dependent transport in the early secretory pathway. Further, this interaction depended on both the
67 headgroup and the backbone of the sphingolipid [8].

68 Cytokinesis is the final step in cell division that divides one cell into two daughter cells. During
69 cytokinesis, an actomyosin contractile ring is formed that is positioned midway between the
70 segregated chromosomes. Narrowing of this ring with the addition of membrane in a
71 spatiotemporally defined mode produces a cleavage furrow that physically divides the cytoplasm
72 [9]. During somatic cytokinesis, the two daughter cells are interconnected *via* intercellular bridges
73 prior to abscission. Although these structures are transient, they accumulate defined lipid species
74 to mediate correct cell division [10-12]. Unlike somatic cytokinesis, in testis, the developing
75 spermatogonial cells divide synchronously with an incomplete cytokinesis where all the daughter
76 cells remain interconnected by cytoplasmic bridges. Thus, the spermatogonial cells develop as a
77 syncytium and become separated from each other only at the end of spermatogenesis during
78 spermatid individualization. The high degree of membrane curvature necessary for cleavage
79 furrow ingression and stabilization of intercellular bridges (ICB)/cytoplasmic bridges necessitates
80 lipid components with specific biophysical properties. While the presence of very long chain fatty
81 acids (which are components of sphingolipids and glycosphingolipids) in cytokinesis has been
82 shown, the relationship between membrane lipid composition, ring constriction and furrow
83 ingression is still underexplored. Although sphingomyelins containing very long chain
84 polyunsaturated fatty acids (VLC-PUFAs) were identified in various mammalian testes including
85 humans, their direct role in spermatogenesis particularly in meiotic cytokinesis remains unknown
86 [13, 14].
87 Ceramide phosphoethanolamine (CPE) is a structural analog of sphingomyelin (SM) in
88 *Drosophila melanogaster*. CPE is synthesized in the luminal compartment of trans Golgi by
89 ceramide phosphoethanolamine synthase (CPES) (Fig.1A). Previously, we have shown that *cpes*
90 null mutants show significant late pupal lethality during development and only about 25% of

91 mutants survive to adulthood. About 60% of *cpes* mutant adults have dorsal closure defects and
92 all the mutant males are sterile. Aged *cpes* mutant adults display light inducible seizures and
93 paralysis due to defective cortex glia [15]. In this study, we show that CPE has unique acyl chain
94 anchors in spermatocytes and is essential for meiotic cytokinesis, spermatid polarity and
95 individualization. The head group of CPE is also important for spermatogenesis. CPES expression
96 in transit amplifying to the spermatocyte stage is essential for successful completion of
97 spermatogenesis. We show that aberrant central spindle behavior, but not mislocalization of PIPs
98 at the cleavage furrows is responsible for the meiotic cytokinesis defect in *cpes* mutants. Further,
99 we show that endocytically retrieved CPE from plasma membrane is enriched in Rab7 positive
100 multivesicular bodies that dock to the ingressing membranes and release intraluminal vesicles in
101 their vicinity. Our results demonstrate the importance of CPE rich membrane addition at the
102 cleavage furrow involving the endocytic pathway.

103 ## Results

104 **Sphingosine with VLC-mono-unsaturated fatty acid and sphingadiene with VLC-saturated**
105 **fatty acid containing sphingolipids are enriched in the testis**

106 To investigate sphingolipid species diversity and their role in *Drosophila* tissues, we performed
107 supercritical fluid chromatography coupled to mass spectrometry (SFC/MS/MS) on lipids from
108 wild type fly head, dissected ovary, and testis (Data S1). As shown in Fig.1B, CPE is a more
109 abundant sphingolipid compared to ceramides (Fig.1C) and hexosylceramides (HexCer) (Fig.1D).
110 The amount of CPE was significantly higher in testis compared to head and ovary (Fig.1B). In
111 contrast hexosylceramides are significantly higher in heads compared to ovary and testis (Fig.1D).
112

113 ***Fig.1. Sphingolipid analysis in wild type Drosophila tissues.*** *(A) De novo sphingolipid*
114 *biosynthetic pathway. De novo sphingolipid biosynthetic pathway begins with condensation of an*
115 *amino acid serine and a fatty acid, lauryl-CoA into 3-ketodihydrosphinganine by serine palmitoyl*
116 *transferase (SPT) complex in the membranes of endoplasmic reticulum (ER). 3-*
117 *ketodihydrosphinganine (3KDS) is reduced to dihydrosphingosine by 3KDS reductase.*
118 *Dihydrosphingosine is acylated to produce dihydroceramide by Schlank. Dihydroceramide is*
119 *desaturated by Δ4 desaturase (DES1) resulting in the formation of ceramide. Ceramide acts as a*
120 *precursor for the biosynthesis of complex sphingolipids both in the ER and Golgi complex.*
121 *Ceramide is actively transported to Golgi by ceramide transfer protein (CERT). In the trans Golgi*
122 *lumen, ceramide is converted to hexosylceramides by GC synthases and to CPE by CPE synthase.*
123 *(B-D) Sphingolipids were extracted from wild type male and female heads and dissected ovaries*
124 *and testes using Methanol:Chloroform method and subjected to SFC/MS/MS. Wild type heads*
125 *from male flies (WTHM), wild type heads from female (WTHF), wild type ovary (WTOY) and wild*
126 *type testis (WTTS). Sphingolipids were quantitated by measuring large fragments in MRM, and*
127 *average amounts from 3 independent biological replicates are shown as picomoles (pmol) in 100*
128 *micrograms of carbon. Each sphingolipid species (CPE (1B), Ceramide (1C) & HexCer (1D)) was*
129 *further subdivided into 5 major subspecies. Each of the subspecies differed in acyl chain length*
130 *but similar in chemical properties: Dihydrosphingosine (DHSPH) base linked to saturated fatty*
131 *acid (SFA) (DHSPH_SFA), Sphingosine (SPH) base linked to SFA (SPH_SFA), Sphingosine*
132 *(SPH) base linked to Monounsaturated fatty acid (MUFA) (SPH_MUFA), Sphingosine (SPH) base*
133 *linked to Polyunsaturated fatty acid (2-6 double bonds, PUFA) (SPH_PUFA) and Sphingadiene*
134 *(SPD) with SFA (SPD_SFA). (E) Cartoon showing the chemical structure of three major CPE*
135 *subspecies including CPE_SPH_SFA, CPE_SPH_MUFA, and CPE_SPD_SFA. (F) CPE*

136 *subspecies within CPE_SPH_SFA that differed in number of carbon atoms in acyl chains of*
137 *sphingosine base and fatty acid. (G) CPE subspecies within CPE_SPH_MUFA. (H) CPE*
138 *subspecies within CPE_SPD_SFA. Statistical significance was calculated using mean, standard*
139 *deviation (SD) and N in Prism 8. The 2way ANOVA multiple comparison was used to calculate P*
140 *values where ****P ≤ 0.0001;***P ≤ 0.001; **P ≤ 0.01; *P ≤ 0.05 and ns P >0.05. Three*
141 *independent biological replicates were performed for each sample and lipids were extracted from*
142 *400 heads or 250 pairs of ovaries or testes for each biological replicate.*
143 Closer examination of acyl chain composition revealed that head and ovary derived CPEs are
144 predominantly composed of sphingosine linked to saturated fatty acid (SPH_SFA) (Fig.1E and
145 1F). Interestingly, in addition to SPH_SFA, CPE in the testis is enriched in two distinct species
146 with net two double bonds in their acyl chain composition including sphingosine (one double
147 bond) linked to mono-unsaturated fatty acid (SPH_MUFA) (Fig.1E and 1G) and a sphingadiene
148 (two double bonds) linked to saturated fatty acid (SPD_SFA) (Fig.1E and 1H). The fatty acid acyl
149 chain lengths of these CPE species are predominantly composed of C20, C22, C24 and therefore
150 could be classified as very long chain (VLC) sphingolipids. The sphingoid base acyl chain length
151 is composed of d14 and d16 (Fig.1G and 1H). The corresponding ceramide precursors are also
152 evident in the wild type testis samples indicating acyl chain diversity is likely introduced during
153 ceramide synthesis but not after CPE synthesis (Fig.1C and Data S1). Remarkably, SPH_MUFA
154 and SPD_SFA are also present in HexCer but at significantly lower levels in the testis compared
155 to heads (Fig.1D vs Fig.1B). The fatty acid acyl chain length of HexCer_SPH_MUFA and
156 HexCer_SPD_SFA showed that they are predominantly composed of C18 and C20 while the
157 sphingoid base is composed of primarily d14 and d16 (Fig.S1B, S1D and S1E). HexCer with d14
158 sphingosine base and C22 PUFA (SPH-PUFA) is enriched in heads compared to testis (Fig.1D,

159 Fig.S1C and S1E). Taken together, these results suggest that CPE in the testis and the HexCer in
160 the central nervous system have unique acyl chain composition.

161 ***Fig.S1. Comparison of hexosylceramide subspecies in Drosophila tissues.*** *(A) Hexosylceramides*
162 *composed of sphingosine base linked to saturated fatty acid (HexCer_SPH-SFA) and its*
163 *subspecies are shown as picomols (pmol) in 100 micrograms of carbon. Wild type heads from*
164 *male flies (WTHM), wild type heads from female (WTHF), wild type ovary (WTOY) and wild type*
165 *testis (WTTS). (B) Hexosylceramide subspecies composed of sphingosine base linked to*
166 *Monounsaturated fatty acid (HexCer_SPH_MUFA). (C) Hexosylceramide subspecies composed*
167 *of sphingosine base linked to Polyunsaturated fatty acid (HexCer_SPH_PUFA). (D)*
168 *Hexosylceramide subspecies composed of Sphingadiene base linked to Saturated fatty acid*
169 *(HexCer_SPD_SFA). (E) Cartoon showing the representative chemical structure of three major*
170 *and one minor HexCer subspecies including HexCer_SPH_SFA, HexCer_SPH_MUFA,*
171 *HexCer_SPD_SFA and HexCer_SPH_PUFA respectively. Statistical significance was calculated*
172 *using mean, standard deviation (SD) and N in Prism 8. The 2way ANOVA multiple comparison*
173 *was used to calculate P values where ****$P \leq 0.0001$;***$P \leq 0.001$; **$P \leq 0.01$; *$P \leq 0.05$ and*
174 *ns $P > 0.05$. Three independent biological replicates were taken for each sample and lipids were*
175 *extracted from 400 heads or 250 pairs of ovary or testis for each biological replicate.*

176 **CPE deficient males are sterile and show defects in male meiotic cytokinesis, spermatid**
177 **polarity and individualization**

178 To understand the biological significance of the unique CPE species in the testis, we reasoned that
179 the *cpes* null mutant generated by us would serve as a suitable tool since *cpes* mutant males are
180 sterile [15]. Immunostaining of *cpes* mutant testis with antibody to Vasa protein, a germ cell
181 specific conserved RNA helicase [16], showed accumulation of germ cells at the tip of the testis

182 (Fig. 2B) and DNA specific staining with DAPI showed absence of mature sperm in seminal
183 vesicles (data not shown). To investigate cytological defects in *cpes* mutant testis, we performed
184 live testis squash preparation followed by phase contrast microscopy. This method allows for easy
185 identification of almost all of the major stages of spermatogenesis [17]. During meiotic divisions,
186 chromosomes and mitochondria are equally partitioned to each of the four daughter cells.
187 Immediately following meiosis, in the round spermatid stage, mitochondria in each daughter cell
188 aggregate to form a large phase dark structure known as the nebenkern. Round spermatids (onion
189 stage spermatids) are characterized by phase dark nebenkern and phase light nucleus at roughly
190 equal size and at a ratio of 1:1 per daughter cell. The nuclear size of round spermatids are directly
191 proportional to the chromatin content, hence any errors in chromosome segregation during meiosis
192 can lead to variability in nuclear size [18, 19]. Similarly, defects in meiotic cytokinesis following
193 normal chromosome segregation results in cells with two or four nuclei and an abnormally large
194 nebenkern. This change can be easily visualized by phase contrast microscopy and is often used
195 as a diagnostic to detect male meiotic defects [19-25]. As shown in Fig.2D, wild type round
196 spermatids contained an equal sized phase light nucleus and a phase dark nebenkern at a ratio of
197 1:1 per cell within the cyst of 64 cells. In contrast, *cpes* mutant round spermatids showed four
198 regularly sized nuclei (tetranucleate) and one abnormally large nebenkern, indicating a failure in
199 cytokinesis in both meiosis I and II divisions (Fig.2E). Quantification of this defect suggest 80%
200 of the round spermatids show tetranucleate and about 20% show two nuclei (Fig.2M). We did not
201 observe single nucleated round spermatids *in* cpes mutant testes (Fig.2M). This defect is unique to
202 male meiotic cytokinesis since larval neuroblasts undergoing asymmetrical mitotic division do not
203 show defects in cytokinesis (Movie S1). Females are largely fertile indicating normal oogenesis
204 (data not shown). Also, even during spermatogenesis we do not observe any defect in the formation

205 of 16 cell staged spermatogonia/spermatocytes indicating that mitotic cytokinesis even in the testis
206 of *cpes* mutants, is not compromised.

207 ***Fig.2. Cytological, immunofluorescence and sphingolipid analyses in cpes mutants.***

208 *(A-C) Whole mount of Drosophila testis immunostained for germ cell specific Vasa protein*
209 *primary antibody and Alexa Fluor 488 secondary antibody (Green) and DNA with DAPI (Blue) to*
210 *visualize various stages of germ cells including stem cells, spermatogonia and spermatocytes (A)*
211 *w^{1118}, (B) cpes mutant and (C) Tub-Gal4>UAS-CPES rescue. (D-F) Phase contrast microscopy of*
212 *live testis squash preparations to visualize round/onion stage spermatids (D) w^{1118}, (E) cpes*
213 *mutant and (F) Tub-Gal4>UAS-CPES rescue. (G-I) Testis squash preparation followed by fixation*
214 *and immunostaining to visualize early elongating spermatids. Arrow indicates spermatid head*
215 *stained with DAPI (Blue) for DNA. The beta tubulin primary antibody and Alexa Fluor 568*
216 *conjugated secondary antibody (Red) were used for immunostaining spermatid tails (axonemes),*
217 *w^{1118} (G), cpes mutant (H) and Tub-Gal4>UAS-CPES rescue (I). (J-L) Whole mount Drosophila*
218 *testis immunostained with cleaved caspase specific DCP-1 primary antibody and Alexa Fluor 568*
219 *secondary antibody (Red) to visualize elongated and individualizing spermatids. DAPI stains the*
220 *DNA (Blue). Cystic bulges are shown with arrows and waste bags with arrow heads (J) w^{1118} (K)*
221 *cpes mutant and (L) Tub-Gal4>UAS-CPES rescue. (M) Quantification of meiotic cytokinesis*
222 *defects in cpes mutants. Round spermatid count from 3 independent experiments for W^{1118}*
223 *(n=1600), cpes (n=300) and from 4 independent experiments for tubulin-Gal4 >UAS-CPES*
224 *rescue (n=2000). (N-P) Sphingolipid analysis in lipid extracts of dissected testis, wild type testis*
225 *(WTTS); cpes mutant testis (CPMT) and bam-Gal4>UAS-CPES Rescue testis (ReTS). (N)*
226 *Comparison of CPE and its subspecies between w^{1118}, cpes mutant and ReTS. (O) Comparison of*
227 *ceramide and its subspecies between w^{1118}, cpes mutant and ReTS. (P) Comparison of*

228 *hexosylceramide subspecies between w^{1118}, cpes mutant and ReTS. Statistical significance was*
229 *calculated using mean, standard deviation (SD) and N in Prism 8. The 2way ANOVA multiple*
230 *comparison was used to calculate P values where ****P ≤ 0.0001; ***P ≤ 0.001; **P ≤ 0.01; *P*
231 *≤ 0.05 and ns P >0.05. Three independent biological replicates were taken for each sample and*
232 *250 pairs of testes were used for lipid extraction from each biological replicate.*
233 Following the round/onion stage, the 64 interconnected haploid cells in the cyst become highly
234 polarized with the nuclei localizing to one end and the sperm tails (axonemes) growing in the
235 opposite side. These elongating spermatid nuclei face towards the seminal vesicles and the tails
236 grow towards the germline stem cell hub/tip of the testis. As shown in Fig.2G, wild type early
237 elongating spermatids had all the nuclei facing one side and their axonemes growing to the
238 opposite side indicating that they are highly polarized. In contrast, all the elongating spermatids in
239 *cpes* mutant cysts appeared as sickle cell shaped with the nuclei present in the middle-bulged area
240 (occasionally throughout the cyst) and their tails growing on both sides of the cyst (Fig.2H). This
241 data indicates that spermatid polarity is compromised in *cpes* mutants.
242 Individualization is the final stage of spermatid differentiation wherein structures called the
243 individualization complex (IC) containing actin cones assemble at the head/rostral end of
244 elongated spermatids and start moving away from the nuclei towards the tail/caudal end of the
245 cyst. As the IC travels it removes the cytoplasmic contents of the cyst and individualizes each
246 spermatozoon with its own plasma membrane. The extruded cytoplasmic content is collected into
247 a sac like structure called the 'cystic bulge' that forms around the IC. As this process proceeds and
248 the IC and cystic bulge reach the end of the flagella, the actin cones and cytoplasmic contents are
249 extruded in a waste bag, the contents of which are degraded later [26]. Activated caspases have a
250 non-apoptotic role in cystic bulge and the waste bag of individualizing spermatids and are essential

251 for successful spermatid individualization [27]. Immunostaining of wild type testis with cleaved
252 *Drosophila* Caspase 1 (DCP-1) antibody showed elongated spermatids undergoing
253 individualization that contained cystic bulges and waste bags (Fig.2J). In contrast, *cpes* mutant
254 testis showed defectively elongated spermatids and was devoid of cystic bulges and waste bags
255 indicating failure in spermatid individualization (Fig.2K).
256 The meiotic cytokinesis, spermatid polarity and individualization defects of *cpes* mutants are fully
257 penetrant (100%) and ubiquitous expression of wild type cDNA copy of CPES completely rescued
258 all male sterility phenotypes (Fig. 2C, F, I, L, M). As shown in Fig.2F, phase contrast imaging of
259 live testis squash preparations showed 1:1 nebenkern to nucleus ratio indicating rescue of meiotic
260 cytokinesis defect. Further, immunostaining of testis squash preparations with tubulin antibody
261 and DAPI showed that spermatid polarity was completely restored wherein all the nuclei faced
262 one side and their tails faced the other side of the cyst (Fig.2I). DCP-1 staining showed
263 individualizing spermatids with cystic bulges and waste bags indicating normal individualization
264 (Fig.2L).
265 To investigate the sphingolipid content in *cpes* mutant, we dissected wild type, *cpes* mutant and
266 germ cell specific rescue (*bam*-Gal4> UAS-CPES) testes, sphingolipids were extracted and
267 analyzed by SFC/MS/MS as described in the methods (Data S1). The mutant and rescue samples
268 were processed at the same time as the wild type for mass spectrometry, hence the wild type testis
269 sample is the same as in Fig.1 (Data S1). There was complete loss of CPE in *cpes* mutant testis
270 (Fig.2N) and expression of CPES only in the germ cells was sufficient to restore CPE to near wild
271 type levels. Loss of CPE synthesis in *cpes* mutants caused concurrent accumulation of ceramides
272 particularly SPH_MUFA and SPD_SFA species (Fig.2O) and expression of CPES in germ cells
273 reduced ceramide levels. HexCer levels were also slightly increased in *cpes* mutant testis (Fig.2P).

274 Interestingly, expression of CPES in germ cells did not reduce the HexCer levels indicating their
275 levels did not correlate with the *cpes* mutant phenotypes in the testis.

276 **CPES enzymatic activity is required for spermatogenesis and accumulation of ceramide is**
277 **not the cause for spermatogenesis defects**

278 To determine whether enzymatic activity of CPES is required for spermatogenesis we generated
279 an active site mutant of CPES. CPES has a conserved amino acid motif $D(X)_2DG(X)_2$ $(A/Y)R(X)_{8-}$
280 $_{16}G(X)_3D(X)_3D$ in the CDP-alcohol phosphotransferase domain (CAPT) [28]. The final aspartates
281 of this motif were shown to be essential for catalysis of human choline/ethanolamine
282 phosphotransferase CEPT1 [29, 30]. We substituted the last two active site aspartates of CPES
283 with alanine residues and subcloned into pUAST vector for generating transgenic flies. The
284 UAS_CPES (DX_3D to AX_3A) mutant transgene was expressed in *cpes* mutant background using
285 *bam*-Gal4 to test if rescue of spermatogenesis phenotypes could be rescued. As shown in Fig.S2A
286 and B, the active site mutant did not rescue spermatogenesis phenotypes suggesting a crucial role
287 for CPES enzymatic activity in spermatogenesis.

288 ***Fig.S2. CPES enzymatic activity is required for spermatogenesis and accumulation of ceramide***
289 ***is not responsible for cpes mutant phenotypes.*** *(A, C and E) Live testis squash preparation*
290 *followed by phase contrast microscopy of round spermatids, (B, D and F) are immunofluorescence*
291 *images of early elongating spermatids from samples corresponding to A, C and E respectively.*
292 *Immunostaining was performed with beta tubulin primary antibody and Alexa Fluor 568*
293 *conjugated secondary antibody (Red). Nuclei are stained with DAPI (Blue) (A and B), the UAS-*
294 *CPES active site mutant (GX_3DX_3D to GX_3AX_3A) was expressed using bam-Gal4 in cpes mutant*
295 *background. (C and D), cpes; dcert^1 double mutants. (E and F) The UAS CDase (neutral*
296 *ceramidase) was expressed using bam-Gal4 driver in cpes mutant background.*

297 We next investigated whether accumulation of ceramide at the Golgi is responsible for the
298 observed phenotypes. Ceramide is generated in the membranes of endoplasmic reticulum (ER) *via*
299 the *de novo* biosynthetic pathway catalyzed by the rate limiting enzyme serine palmitoyltransferase
300 (SPT) (Fig.1A). Subsequently ceramide is actively transported from ER to Golgi *via* ceramide
301 transfer protein (DCERT) and thus absence of DCERT could prevent ceramide accumulation at
302 the Golgi (Fig.1A) [31]. To investigate whether blocking ceramide transport from ER to Golgi
303 could restore spermatogenesis, we generated *cpes* and $dcert^{1}$ double mutants and their testes were
304 analyzed for meiotic cytokinesis and spermatid polarity phenotypes. However, as shown in
305 Fig.S2C and D, *cpes*; $dcert^{1}$ double mutants did not rescue meiotic cytokinesis and spermatid
306 polarity indicating ceramide accumulation at the Golgi (due to lack of CPES activity in the Golgi)
307 may not be responsible for *cpes* mutant phenotypes. In *Drosophila*, transgenic expression of
308 neutral ceramidase was shown to reduce ceramide levels *in vivo* [32]. We overexpressed
309 ceramidase (UAS CDase) in germ cells using *bam*-Gal4 in *cpes* mutant background and testes
310 from the resulting progeny were analyzed for the rescue of mutant phenotypes. However,
311 expression of CDase did not rescue meiotic cytokinesis and spermatid polarity (Fig.S2E and F),
312 suggesting that absence of CPE but not accumulation of ceramide is responsible for the
313 phenotypes.

314 **Transcriptomic and genetic dissection of spatiotemporal role of CPES in spermatogenesis**

315 Spermatogenesis is a highly conserved process across various taxa that is facilitated by highly
316 dynamic transcriptome. An earlier study leveraged single cell RNAseq and unsupervised
317 clustering to identify all the major cell classes of the sperm lineage and validated them with
318 previously studied marker genes [33]. To characterize cell type specific transcriptional signatures
319 in *cpes* mutants *in vivo*, we performed total RNA-seq with dissected testis from w^{1118}, *cpes* mutant

320 and *bam*-Gal4>UAS CPES rescue. Using Gene Set Enrichment analysis (GSEA) we compared
321 our RNAseq results with the top 50 expressed genes from each cell type/cellular status that were
322 previously classified to confirm the presence of germline stem cells (GSC), spermatogonia,
323 spermatocytes, and spermatids (germ cells) as well as cyst stem cells, terminal epithelial cells and
324 hub cells (somatic cells) [33]. We found that gene sets corresponding to GSC, early spermatogonia
325 and late spermatogonial cells are enriched in *cpes* mutants compared to wild type and rescue testis
326 (Fig.S3). In contrast, gene sets corresponding to early and later spermatocytes, early, and mature
327 spermatids are enriched in wild type and rescue testis compared to *cpes* mutant testis (Fig.S3).
328 These results suggested that CPES might play important roles during late spermatogonial, early
329 and late spermatocyte stages for successful completion of spermatogenesis.

330 ***Fig.S3. Analysis of cell type specific transcriptomic signatures in cpes mutants:*** *(A) GSEA using*
331 *top 50 cell type specific expressed gene sets and compared between cpes versus wild type (WT)*
332 *and bam-Gal4>UAS CPES rescue (Rescue). Red bars indicate gene sets enriched in cpes mutants*
333 *and blue bars indicate gene sets enriched in WT & Rescue. (B) enrichment plots for each of the*
334 *cell type shows the distribution of individual genes in each set (vertical lines on red to blue parallel*
335 *bar). Genes with positive enrichment score (ES) indicate that they are enriched in cpes mutants*
336 *whereas negative enrichment score indicate that they are enriched in WT and Rescue. (C)*
337 *Heatmap comparison of cell type specific enriched gene sets in w wild type (W1118), cpes and*
338 *Rescue (bam-Gal4>UAS CPES rescue). Red indicates gene sets enriched in cpes mutants and blue*
339 *indicate gene sets enriched in WT & Rescue.*

340 To determine the stage of germ cell differentiation at which CPES expression has an important
341 role, we performed cell type/stage specific rescue experiments using UAS/Gal4 system in the *cpes*
342 mutant background (Fig.3A). We first expressed UAS-CPES in cyst cells using C587-Gal4 to

343 investigate a possible non-cell autonomous role. C587-Gal4 was expressed in all early somatic
344 cells at the apical tip of the testis including somatic cyst stem cells and cyst cells (Fig.S4 D &H)
345 [34]. As shown in Fig.3, expression of wild type CPES in cyst cells did not rescue meiotic
346 cytokinesis, spermatid polarity or individualization defects (Fig.3 B, F and J respectively). We
347 next expressed wild type UAS-CPES in germ cells using three different Gal4 drivers that have
348 been previously shown to be specifically expressed in stem cells (*nos*-Gal4), transit amplifying
349 spermatogonial cells (*bam*-Gal4) and early spermatocytes (*chif*-Gal4) (Fig.3A). Na*nos* (*nos*) gene
350 encodes for an RNA-binding protein involved in formation of translational repressor complex. It
351 is required for germ plasm organization, germline development, germline stem cell renewal and
352 neuronal morphogenesis [35]. To specifically express a transgene of interest in male and female
353 germline stem cells *nanos*-Gal4-VP16 was routinely used. This construct consists of 700bp *nos*
354 promoter, Gal4-VP16 ORF, *nos* 3' UTR and 500bp of 3' genomic *nos* transcription unit. In male
355 germ line *nos*-Gal4 primarily expresses in GSC and early spermatogonial stages [36]. Bag of
356 marbles (*bam*) gene encodes for a fusome (a germ cell specific organelle) associated protein. The
357 Bam protein is required for activation of the switch from spermatogonia to spermatocytes. The
358 construct *bam*-Gal4-VP16 has been successfully used to drive the expression of transgenes in late
359 spermatogonia and early spermatocytes in *Drosophila*. This construct consists of 900bp bam
360 promoter, 500bp *bam* 5'UTR, Gal4:VP16 ORF and HSP70 3'UTR. Although transgenes driven
361 with *bam*-Gal4-VP16 express in late spermatogonia through early spermatocytes, the peak
362 expression was shown to occur during spermatocytes [37]. Gene trap Gal4 insertion collection
363 screen identified *Chiffon*-Gal4 to drive transgene expression specifically in early spermatocytes
364 and somatic cysts cells [38]. To verify the expression pattern of these Gal4 drivers in our
365 experimental settings we have crossed *nos*-Gal4 (BDSC#4937) with various pUASP/pUAST-GFP

366 tagged proteins including pUASP-*alpha-Tubulin*-GFP, pUAST-EGFP, and pUAST-PLCδ-PH-
367 EGFP. As expected, *nos*-Gal4 expression is restricted to early germ cells present at the tip of the
368 testis including germline stem cells (GSCs) and early spermatogonial cells (Fig.S4A, E & I). On
369 the contrary, *bam*-Gal4 expression is strong just below the testis tip where spermatogonia and early
370 spermatocytes are expected to be present (Fig.S4B, F & J). However, depending on the stability
371 of the expressed protein *bam*-Gal4 mediated expression is either restricted to spermatogonia and
372 early spermatocytes (eg. PLCδ-PH-EGFP, Fig.S4J) or persisted through later stages including
373 early, later spermatocytes and even in spermatids (eg. *Alpha tubulin* and EGFP, Fig.S4B & F).
374 Expression of *chif*-Gal4 expression was detectable in spermatocytes (Fig.S4C) but more strongly
375 in elongated spermatids (Fig.S4G & K). Interestingly, As shown in Fig.3, we observed varying
376 degree of rescue, depending on the germ cell differentiation stage at which UAS-CPES was
377 expressed. The *nos*-Gal4 dependent expression of UAS-CPES partially rescued both meiotic
378 cytokinesis (Fig.3C and N) and spermatid polarity (Fig.3G) however, individualizing spermatids
379 lacked cystic bulges and waste bags indicating individualization was not fully rescued (Fig.3K).
380 The *bam*-Gal4 dependent expression of UAS-CPES in transit-amplifying cells completely rescued
381 meiotic cytokinesis (Fig.3D, and N) and spermatid polarity, and individualizing spermatids
382 contained cystic bulges and waste bags (Fig.3H and L). In contrast, only partial rescue of meiotic
383 cytokinesis was observed when UAS-CPES was expressed in spermatocytes using *chif*-Gal4
384 (Fig.3E & 3N). Although spermatid polarity was completely rescued, the individualizing
385 spermatids largely lacked cystic bulges and waste bags indicating that individualization was
386 defective (Fig.3I and M).

387 ***Fig.3. Genetic dissection of spatiotemporal role of CPES in spermatogenesis.*** *(A) Schematic*
388 *illustration of early germ cell differentiation and stage specific Gal4 expression patterns. (B-E)*

389 *Phase contrast microscopy of round spermatids in live testis squash preparations. (F-I) Early*
390 *elongating spermatids immunostained for beta tubulin primary antibody (Red) and DAPI for DNA*
391 *(blue) (J-M) Individualizing spermatids immunostained for cleaved caspase DCP-1 antibody*
392 *(Red) and DAPI for DNA(Blue). (B, F and J) C587-Gal4 drives the expression of UAS-CPES in*
393 *cyst cells of cpes mutants. (C, G and K) Nanos-Gal4 drives the expression of UAS-CPES in GSCs*
394 *and spermatogonia. (D, H & L) bam-Gal4 drives the expression of UAS-CPES in 4-16 cell stages*
395 *of spermatogonia and spermatocytes (E, I & M) chif-Gal4 drives the expression of UAS-CPES in*
396 *early spermatocytes. (N) Measurement of cytokinetic defects in testis squash preparations in cyst*
397 *and germ cell specific rescue samples. Round spermatid count from 4 independent experiments for*
398 *C587-Gal4 >UAS-CPES (n=500), 6 independent experiments nos-Gal4 >UAS-CPES (n=2500),*
399 *5 independent experiments for bam-Gal4 >UAS-CPES (n=2500), and 6 independent experiments*
400 *for chif-Gal4 >UAS-CPES (n=3000). (O) Male fertility test where individual male from each of*
401 *the UAS-CPES rescue experiment was crossed with 3 wild type females. The vials which produced*
402 *at least 5 pupae or progeny were counted as fertile and plotted as percent fertility compared to*
403 *wild type males. (P-S) Whole mount immunostaining followed by confocal imaging of genomic*
404 *CPES flies where CPES is tagged with V5 at the C-terminus (red). GM130 is a cis-Golgi marker*
405 *(green) and DAPI (blue) stains the DNA.*

406 ***Fig.S4. Cell type specific expression pattern of various UAS and Gal4 constructs in Drosophila***
407 ***testis.*** *(A-) Whole mount Drosophila testis immunostained GFP with anti-GFP antibody (Green),*
408 *DAPI stains DNA (Blue). (A) nanos-Gal4 (nos) drives the expression of pUASP-αTubulin-GFP,*
409 *(B) bam-Gal4 drives the expression of pUASP-alphaTubulin-GFP, (C) chiffon-Gal4 drives the*
410 *expression of alpha-Tubulin-GFP, (D) C587-Gal4 drives the expression of alpha-Tubulin-GFP,*
411 *(E) nanos-Gal4 (nos) drives the expression of pUAST-EGFP, (F) bam-Gal4 drives the expression*

412 *of pUAST-EGFP, (G) chiffon-Gal4 drives the expression of pUAST-EGFP, (H) C587-Gal4 drives*
413 *the expression of alpha-Tubulin-GFP, (I) nanos-Gal4 (nos) drives the expression of pUAST-PLCδ-*
414 *PH-EGFP, (J) bam-Gal4 drives the expression of pUAST-PLCδ-PH-EGFP, (K) chiffon-Gal4*
415 *drives the expression of pUAST-PLCδ-PH-EGFP, (L-N) Verification of various nanos-Gal4*
416 *drivers and their expression pattern. BDSC#4937 (used in this study) and BDSC#64227*
417 *specifically express transgene in GSC and early spermatogonia compared to BDSC#32563 which*
418 *expresses more broadly.*
419 To determine the extent to which male fertility was rescued by cell type specific CPES expression
420 compared to wild type, we performed male fertility tests. As shown in Fig.3O, expression of UAS
421 CPE in transit amplifying spermatogonial cells and spermatocytes (*bam*-Gal4) rescued male
422 fertility to wild type levels. In contrast only partial rescue was observed when UAS-CPES was
423 expressed only in stem cells (*nos*-Gal4) or in spermatocytes (*chif*-Gal4). Expression of UAS-
424 CPES in cyst cells (C587-Gal4) did not rescue male sterility as all males were sterile (Fig.3O).
425 To determine *in vivo* CPES localization more precisely at the protein level, we have generated a
426 construct with a 6437 bp extended CPES genomic fragment that was modified by recombineering
427 to carry V5-tag at the C-terminus [15]. Transgenic flies expressing genomic CPES tagged with V5
428 at the C-terminus fully rescued lethality, photosensitive epilepsy and all other phenotypes
429 including spermatogenesis defects. Immunostaining followed by confocal imaging showed that
430 CPES_V5 was highly expressed in the cells that are present just below the tip of the testis (Fig.3P
431 and S). This area of the testis is known to be enriched in late spermatogonia and early
432 spermatocytes [17].

433 Taken together these results show that testis specific CPE generation by CPES from late
434 spermatogonia stage to spermatocyte stage is crucial for successful meiotic cytokinesis, spermatid
435 polarity and spermatid individualization.

436 **Insect CPE Synthases but not Sphingomyelin Synthase rescue male sterility defects**

437 Previously we have shown that CPE has an important structural role in cortex glial plasma
438 membranes [15]. The cortex glial plasma membranes are severely defective in *cpes* mutants
439 leading to loss of cortex glia neuronal cell body interactions during development and increased
440 susceptibility to light inducible epilepsy in adults. Further, we have shown that overexpression of
441 human sphingomyelin synthase 1 (hSMS1) that produces SM instead of CPE was sufficient to
442 rescue cortex glia plasma membrane defects via establishment of detergent resistant membranes.
443 We wondered whether overexpression of hSMS1 could also rescue the spermatogenesis
444 phenotypes of *cpes* mutant. To this end, UAS-hSMS1 was ubiquitously expressed using tubulin-
445 Gal4 in *cpes*, the adult male testes were dissected, and live testis squash preparations were
446 observed using phase contrast microscopy. However, as shown in Fig.S5A, hSMS1
447 overexpression did not rescue male meiotic cytokinesis. Further, immunostaining analysis showed
448 that spermatid polarity was also not rescued (Fig.S5E) suggesting an important role for the CPE
449 head group in spermatogenesis. We next investigated whether expression of other insect derived
450 CPES could rescue *cpes* mutant phenotypes. To test this, we ubiquitously expressed *Aedes aegypti*
451 (Yellow fever mosquito, amino acid sequence shows 60% identity and 77% similarity), and
452 *Bombyx mori* (domestic silk moth, amino acid sequence shows 43% identity and 58% similarity)
453 derived UAS-CPES homologs in *cpes* mutant background using tubulin-Gal4. As shown in Fig.S5
454 mosquito and silk moth CPES were able to completely rescue defects in meiotic cytokinesis
455 (Fig.S5B-D) and spermatid polarity (Fig.S5F and G respectively).

456 ***Fig.S5. Insect CPE synthases but not sphingomyelin synthases rescue spermatogenesis defects.***
457 *(A-C) Phase contrast microscopy of round spermatids where UAS hSMS1 (A), UAS Aedes CPES*
458 *(B), and UAS Bombyx CPES (C) were ubiquitously expressed in cpes mutant background using*
459 *tubulin Gal4. The scale bar is equivalent to 10 μm. (D) Measurement of cytokinetic defects in*
460 *UAS-hSMS1, UAS-Aedes aegypti and UAS-Bombyx mori CPES rescue testes. 4 independent*
461 *experiments for UAS-hSMS1 (round spermatid count, n=500), 2 independent experiments for*
462 *UAS-Aedes aegypti (round spermatid count, n=1100) and 4 independent experiments for UAS-*
463 *Bombyx CPES (round spermatid count, n=1900). (E-G) Confocal images of elongating spermatids*
464 *immunostained with beta tubulin primary antibody and Alexa Fluor 568 secondary antibody (Red)*
465 *and DAPI for DNA (Blue). The UAS hSMS1 (E), UAS Aedes CPES (F) and UAS Bombyx CPES*
466 *(G). (H-K) Sphingolipid analysis of lipids extracted from testis of wild type, cpes mutant, and*
467 *various rescues expressed in germ cells using vasa-Gal4. In contrast to Figs.1 and 2, here we used*
468 *whole male organ (testis, accessory glands, collecting ducts and ejaculatory bulb) for lipid*
469 *extraction. (H) The amounts of CPE and its subspecies in wild type, cpes mutant and various*
470 *rescues are shown. (I) Ceramide and its subspecies are shown in picomoles per 100μg of carbon.*
471 *(J) Hexosylceramide subspecies amounts are shown in bar diagram. (K) Amount of sphingomyelin*
472 *(SM) and its subspecies are shown as picomoles per 100μg of carbon. Fluorescent blue green part*
473 *of the bar represents SM species with net two double bonds in them. (L) Thin layer*
474 *chromatography (TLC) of lipids extracted from 50 pairs of testes from each genotype. The position*
475 *of SM on TLC is indicated by an arow. Dihydrosphingosine (DHSPH), Sphingosine (SPH),*
476 *Sphingadiene (SPD) Saturated fatty acid (SFA), Monounsaturated fatty acid (MUFA) and*
477 *polyunsaturated fatty acid (PUFA). Statistical significance was calculated using mean, standard*
478 *deviation (SD) and N in Prism 8. The 2way ANOVA multiple comparison was used to calculate P*

479 *values where ****P ≤ 0.0001;***P ≤ 0.001; **P ≤ 0.01; *P ≤ 0.05 and ns P >0.05. Three*
480 *independent biological replicates were taken for each sample and lipids were extracted from 250*
481 *male organs for each biological replicate.*
482 To investigate the nature of sphingolipid species synthesized by hSMS1, *Aedes aegypti*, *Bombyx*
483 *mori* derived CPES, we specifically expressed these transgenes in germ cells using *vasa*-Gal4,
484 their male reproductive system was dissected, lipids were extracted and subjected to sphingolipid
485 analysis using SFC/MS/MS as described in the methods section (Data S2). As shown in Fig.S5H
486 germ cell specific expression of *Drosophila* CPES, *Bombyx mori* CPES completely restored CPE
487 to the wild type amounts. *Aedes aegypti* CPES also synthesized significant amount of CPE but to
488 a lower amount than *Drosophila* CPES. However, all three distinct CPE species are synthesized
489 by *Aedes aegypti* CPES and *Bombyx* CPES (Fig.S5H). As anticipated, hSMS1 did not synthesize
490 CPE, but produced significant amount of SM (Fig.S5K). However, the amount of SM is relatively
491 low compared to CPE, perhaps due to limited expression/stability of hSMS1 in germ cells (vasa-
492 Gal4). Indeed, ubiquitous expression of hSMS1 using actin-Gal4 driver significantly increases the
493 SM amounts (Fig.S5L). However, expression of hSMS1 with ubiquitous drivers like actin-Gal4
494 and tubulin-Gal4 did not rescue the spermatogenesis (Fig.S5A and E; data not shown for actin-
495 Gal4) suggesting the importance of the CPE head group. We next analyzed the ceramide content
496 in these samples and found that ceramide levels were significantly high in *cpes* mutants and
497 hSMS1 rescue compared to *Drosophila* CPES rescue (Fig.S5I). However, as discussed in Fig.S2
498 higher ceramide content might not contribute to the cytokinetic defects in *cpes* mutants. Similarly,
499 higher amounts of HexCer in *Aedes aegypti* CPES rescue and *Bombyx mori* CPES rescue also did
500 not correlate with the rescue of spermatogenesis phenotypes (Fig.S5J). Taken together these results

501 suggest that the *Drosophila* spermatogenesis is strictly dependent on CPE and the head group of
502 CPE play an important role.

503 **Aberrant central spindle behavior but not localization of PIPs at the plasma membrane is**
504 **responsible for defective meiotic cytokinesis in *cpes* mutants**

505 Precise organization of central spindle microtubule is not only required for initial cleavage furrow
506 formation but also for maintenance of contractile structures during furrow ingression. Several
507 microtubule interacting proteins including Fascetto, kinesin 6 family member MKLP1/Pavarotti
508 (pav), chromokinesin klp3A, Orbit etc., are enriched in the central spindle midzone and are
509 essential for cytokinesis [39]. To determine the transcriptional signatures relating to spindle
510 organization and function in our RNAseq data, we performed GSEA pathway comparisons
511 between w^{1118} (WT), *cpes* (KO) and rescue (RES) samples. As shown in Fig.S6A. we found several
512 pathways including spindle organization, metabolism, endocytosis, signaling, male meiotic
513 cytokinesis, spermatid differentiation, sperm individualization etc., are significantly altered in *cpes*
514 mutants (Fig. S6A). Red bars in the Fig. S6A indicate gene sets enriched in *cpes* mutants and blue
515 bars indicate gene sets enriched WT & RES. GSEA showed many genes involved in spindle
516 elongation and spindle organization are positively correlated with the mutant phenotype (Fig. S6B
517 & E). The heat map comparison for genes involved in spindle organization and elongation are
518 shown (Fig.S6). Several of the genes implicated in spindle organization have also been annotated
519 under those for spindle elongation and hence appear under both categories. However, as shown in
520 Fig.S3 relative enrichment of earlier stages compared to later stages limits the accurate prediction
521 of altered pathways in *cpes* mutants.

522 *Fig.S6. GSEA pathway analysis indicates enrichment of spindle elongation and spindle elongation*
523 *processes. (A) GSEA pathway analysis of RNA seq data from w^{1118}, cpes mutant and bam-*

524 *Gal4>UAS-CPES rescue testis. Three independent biological replicates were taken for each*
525 *sample and RNA was extracted from 200 pairs of testes for each biological replicate. (B)*
526 *Enrichment plot showing genes involved in spindle elongation are positively correlated in cpes*
527 *mutants compared to* w^{1118} *and bam-Gal4>UAS-CPES rescue. (C-D) Heatmap shows spindle*
528 *elongation genes are enriched in cpes mutants. (E) Enrichment plot showing genes involved in*
529 *spindle organization are positively correlated in cpes mutants compared to* w^{1118} *and rescue. (F-*
530 *G) heat maps show top 100 enriched genes in cpes mutants (H) Heatmap shows the top 50 genes*
531 *enriched in wild type and rescue.*
532 To better study spindle behavior during male meiotic cytokinesis *in vivo*, we performed live
533 imaging on isolated cysts. We first dissected the testis in M3 insect cell culture media and cut open
534 the muscle sheath to release intact spermatocyte cysts into the media. Subsequently, we transferred
535 spermatocyte cysts to poly-D-lysine coated cover glass dishes and performed live imaging using
536 Andor spinning disk confocal microscopy as described in the methods section. We chose mCherry
537 tagged microtubule cross linking protein Feo (Ubi-p63E-*feo*-mCherry) as a marker for central
538 spindle. Feo-mCherry was shown to accumulate at the anaphase B and telophase central spindle
539 [40]. We also used spaghetti squash (sqh) gene encoding myosin II regulatory light chain (RLC)
540 tagged to GFP (*sqh*-GFP-RLC) as a marker for the actin-myosin based structure known as
541 contractile ring that assembles during late anaphase [41]. The actin and myosin ring positioned
542 midway between two spindle poles is thought to drive the formation of the cleavage furrow during
543 telophase. As shown in Movie S2, Fig.4A, the actomyosin ring (*sqh*-GFP-RLC) quickly assembles
544 around the central spindle during late anaphase and both simultaneously constrict through early to
545 late telophase. At the end of late telophase *feo*-mCherry disassembles however, *sqh*-GFP-RLC
546 remains and becomes part of ring canal/cytoplasmic bridges between daughter cells (Movie S2).

547 Interestingly, in *cpes* mutants, the initial assembly of central spindle and actomyosin ring occurred
548 normally (Movie S3) however, central spindle and actomyosin ring constriction became uneven
549 since there is barely any furrow ingression and led to substantial disengagement between the
550 contractile ring and the central spindle during meiosis (Fig.4A). As a result, the central spindle and
551 actomyosin ring disassembled prematurely (Movie S3). Quantification of this behavior suggested
552 that more than 80% of the spermatocytes showed detachment of the contractile ring and central
553 spindle (Fig.4B). Other minor variations included the contractile ring detaching from the plasma
554 membrane, contractile ring sliding and dumping to one end and the contractile ring and central
555 spindle being destabilized simultaneously at one end (Fig.4B). Expression of UAS-CPE in germ
556 cells was sufficient to rescue this phenotype (Movie S4, Fig.4A).

557 ***Fig.4. Aberrant central spindle behavior but not localization of PIPs at the plasma membrane***
558 ***is responsible for meiotic cytokinesis defect in cpes mutants.*** *(A, C & D) Snapshots of live*
559 *spermatocytes undergoing meiosis I cytokinesis. In horizontal view (left), one slice of a z-stack*
560 *was shown. In cross-sectional view across cleavage furrow, maximum intensity projection image*
561 *was shown (right). Control spermatocytes (top row), cpes mutant spermatocytes (middle row) and*
562 *tubulin-Gal4>UAS-CPES rescue (bottom row). (A) Spermatocytes expressing myosin II*
563 *regulatory light chain tagged to GFP under its own promoter (sqh) that localizes to contractile*
564 *ring and mCherry tagged fascetto (feo) under the control of Ubi-p63E promoter that binds to*
565 *central spindle microtubules. (B) Quantification of spindle organization defects, central spindle*
566 *(CS) detachment from contractile ring (CR), detachment of CR from plasma membrane (PM), CR*
567 *slides on PM and CS and CR destabilizing from end (C) Spermatocytes expressing GFP tagged*
568 *pleckstrin homology (PH) domain of PLCD (UAS-PLCδ-PH-EGFP) under the control of Tub-*
569 *Gal4 that localizes to plasma membrane in the presence of phosphatidylinositol-4,5-bisphosphate*

570 *(PIP2) and Ubi-p63E-feo-mCherry. (D) Spermatocytes expressing GFP tagged PH domain of*
571 *steppke/Grp1 under the control of alpha Tub84B promotor (tGPH) that localizes to plasma*
572 *membrane in the presence of phosphatidylinositol-3,4,5-triphosphate (PIP3) and Ubi-p63E-Feo-*
573 *mCherry.*
574 Previous studies have shown that phosphatidylinositols (PIP) play critical roles in somatic and
575 meiotic cytokinesis [42]. Further, in mammalian (HeLa) cells undergoing mitosis, sphingomyelin-
576 rich lipid domains in the outer leaflet of cleavage furrow were shown to be required for
577 accumulation of PIP2 to the cleavage furrow which in turn is required for proper translocation of
578 RhoA and progression of cytokinesis. We wondered whether the distribution of PIP at the plasma
579 membrane or at the cleavage furrow is altered in *cpes* mutants during meiosis. To investigate PIP
580 distribution in *cpes* mutant membranes we used PIP2 reporter UAS-PLCδ-PH-EGFP (UAS
581 regulatory sequence drives expression of EGFP fused to the PH domain of human PLCdelta 1) and
582 PIP3 reporter tGPH (an alphaTub84B promoter drives the expression of EGFP fused to the PH
583 domain of Steppke) [43, 44]. The PIP2 reporter PLCδ-PH-EGFP was shown to uniformly localize
584 to the entire membrane including cleavage furrow in *Drosophila* spermatocytes [45]. Indeed, we
585 have seen similar uniform distribution in both control and *cpes* mutant spermatocyte plasma
586 membranes indicating normal distribution of PIP2 (Movie S5 and S6, Fig.4C). Live imaging
587 analysis on *cpes* mutant spermatocytes expressing PLCδ-PH-EGFP revealed normal cleavage
588 furrow initiation, but progression of furrow failed due to the disconnect between central spindle
589 and the furrow (Movie S6, Fig.4C). Expression of wild type CPES restored this phenotype (Movie
590 S7, Fig.4C). Of note, PLCδ-PH-EGFP localization to spermatocyte plasma membrane was
591 significantly reduced upon loss of cyst cells although this acute reduction did not prevent
592 spermatocytes from completing cytokinesis during meiosis 1. We next investigated the PIP3

593 distribution in control meiotic spermatocytes using tGPH. Interestingly, we found that tGPH
594 localized to plasma membranes and became significantly enriched at cleavage furrows (Movie S8,
595 Fig.4D). Of note, even here, we have observed that plasma membrane localization and cleavage
596 furrow enrichment of tGPH strictly depended on the intact cyst. While it is currently unknown if
597 PIP3 localization to the spermatocyte cleavage furrows has any impact on cytokinesis, a recent
598 study has shown that cytohesin Steppke reduces tissue tension by inhibiting the actomyosin
599 activity at adherens junctions and actomyosin network assembly is necessary and sufficient for
600 local Steppke accumulation in *Drosophila* embryos [46]. Next, we wondered if cleavage furrow
601 enrichment of PIP3 is altered in *cpes* mutants. However, as shown in Movie S9, Fig.4D, PIP3
602 localization to the cleavage furrow was not altered but again there was a disconnect between
603 cleavage furrow and central spindle during cleavage furrow ingression. Expression of wild type
604 CPES restored this phenotype (Movie S10; Fig.4D). Overall, these observations suggest that
605 aberrant spindle behavior but not the localization of PIPs to the plasma membrane or cleavage
606 furrow, is responsible for meiotic cytokinesis defect in *cpes* mutants.

607 **CPE endocytosis and targeting to cleavage furrows occurs during meiotic cytokinesis**

608 To determine how CPE is promoting the synergy between central spindle constriction and cleavage
609 furrow ingression during cytokinesis we have utilized recombinant CPE binding protein tagged
610 with mCherry as a reporter for visualization of CPE on spermatocyte plasma membranes. The
611 mushroom-derived protein of the aegerolysin family pleurotolysin A2 (PlyA2) was shown to
612 specifically bind to CPE and was demonstrated to be a versatile tool for visualizing CPE in live
613 *Drosophila* tissues [47]. We have reevaluated the efficacy of recombinant PlyA2-mCherry protein
614 in detecting endogenous CPE on live spermatocyte membranes. The wild type and *cpes* mutant
615 spermatocytes were treated with 10 μg/ml of PlyA2-mCherry in M3 insect media for 1hour at

616 room temperature, washed with fresh M3 media, and imaged on an Andor spinning disk confocal
617 microscope. As shown in Fig.5A-D, PlyA2-mCherry specifically bound to the plasma membranes
618 of wild type spermatocytes but not to the *cpes* mutant spermatocytes showing specificity of this
619 protein binding to CPE. Interestingly, we found that PlyA2-mCherry was endocytosed in wild type
620 spermatocytes (Fig.5A). To determine the nature of these endosomes where CPE is enriched, we
621 performed live imaging on spermatocytes expressing endogenous EYFP-MYC tagged Rab
622 proteins [48]. The small GTPases Rab4, Rab7 and Rab11 were shown to mark early, late and
623 recycling endosomes respectively [49-51] while Rab6 was shown to be associated with the Golgi
624 membranes [52]. The spermatocytes expressing individual EYFP-Rab proteins were treated with
625 recombinant PlyA2-mCherry and imaged. As shown in Fig.5G, M and P, PlyA2-mCherry
626 colocalized with Rab4, Rab7 and some of the Rab11 endosomes respectively. Colocalization
627 coefficient measurements further support these observations (Fig.5Q). However, PlyA2-mCherry
628 containing structures did not colocalize with Rab 6 positive Golgi membranes (Fig.5J). These
629 results suggested that CPE on spermatocyte plasma membranes is actively targeted to the
630 endocytic pathway. We next wondered whether endosomes carrying CPE migrate to cleavage
631 furrows during meiotic cytokinesis. EYFP-Rab 7 and EYFP-Rab11 were strongly expressed in
632 spermatocytes compared to Rab4 and therefore we followed their dynamics during meiotic
633 cytokinesis. Strikingly, as shown in Fig.6A-F, & Movie.S11, PlyA2-mCherry containing Rab7
634 positive endosomes were actively targeted to cleavage furrows. Similar EYFP-Rab7 localization
635 was seen in intact cysts (Fig.6G-I). The PlyA2-mCherry also colocalized to some of the EYFP-
636 Rab11 recycling endosomes which in turn localized to ingressing membranes at the cleavage
637 furrow (Fig.6J-O and Movie S12). Overall, the endocytosis of CPE and targeting to the ingressing
638 cleavage furrow *via* Rab7 and Rab11 marked endosomes indicates their importance in delivery of

639 lipids to the ingressing membranes of the furrow and coordination of this event with proper spindle
640 behavior and meiotic cytokinesis.
641 To further verify the functional significance of endosome mediated CPE trafficking in cytokinesis
642 we performed genetic experiments involving conditional expression of EYFP-Rab11DN (BDSC#)
643 proteins and Rab7 mutants [53]. Rab11 null mutants die early during development [54]. In that
644 study, it was demonstrated that when spermatocytes enter meiosis 1 as the Golgi disassembles, the
645 Rab11 was shown to be associated with the ER compartment. Rab11 also localizes to vesicles at
646 the cell poles during anaphase and early telophase and at the cell equator during mid- and late
647 telophase. Larval testes of escaper flies carrying Rab11 semi lethal transheterozygote alleles
648 showed abnormal constriction of the contractile rings and a failure of cytokinesis in 10-30% of the
649 flies. We chose to conditionally express dominant negative EYFP-Rab11^{S25N} ubiquitously using
650 Gal80^{ts} and tub-Gal4 to study cytokinetic defects in spermatocytes. The expression of EYFP-
651 Rab11S25N (Rab11 DN) in late 3rd instar larvae was induced by incubation at 30ºC for 4 days.
652 The late pupal gonads were dissected, and cytological analysis was performed to measure percent
653 cytokinetic defects. Consistent with previously published results [54, 55], we found significant
654 increase in cytokinetic defects in Rab11DN expressing gonads (Fig.S7B & E), confirming
655 important roles of Rab11 mediated membrane trafficking during cytokinesis.
656 Rab7-null mutant flies generated by imprecise excision of P-element resulted in a 1025 bp deletion
657 that removed most of the protein coding exon and the 5' untranslated region (UTR) [53]. The
658 mutants displayed late pupal lethality and western blotting with Rab7 antibody confirmed the
659 absence of Rab7 protein in the mutant pupae (Fig.S7C). To investigate meiotic cytokinetic defects
660 in Rab7 mutants we performed testis squash preparations followed by phase contrast microscopy.
661 Interestingly, we found significant increase (15%) in meiotic cytokinesis defects in Rab7 mutants

662 (Fig.S7D & E) compared to wild type controls where cytokinetic defects are virtually zero [54,
663 55] (Fig.S7A), suggesting a significant role for Rab7 in male meiotic cytokinesis. Previous studies
664 have shown that Rab7 protein is required downstream of late endosomes or multivesicular bodies
665 (MVBs) for transfer of cargo to lysosomes [56], therefore formation and migration of late
666 endosomes to the cleavage furrow may not be affected in Rab7 mutants. Although less efficient,
667 we observed that PlyA2-mCherry continued to be endocytosed and targeted to cleavage furrow in
668 Rab7 mutants (Movie S13). The partial cytokinetic defects in Rab7 mutants indicates existence of
669 alternative mechanisms to compensate for loss of Rab7 during cytokinesis. Future experiments
670 with other Rab protein mutants in combination with Rab7 mutants might help address this
671 possibility. The lethal nature of Rab7 mutants during the pupal stage and the time required for
672 inducing Rab11DN during pupal stage posed technical difficulties in creating double mutants and
673 measuring cytokinetic defects in these backgrounds.

674 ***Fig.5.Ceramide phosphoethanolamine (CPE) localizes to plasma membrane and endosomes.***
675 *(A-D) Live spermatocytes were incubated with purified PlyA2-mCherry (10 μg/ml) for 30 min*
676 *followed by washes with M3 insect media (2x) and imaged using spinning disk confocal*
677 *microscopy. (A and B) w^{1118} spermatocytes, (C and D) cpes spermatocytes. (E-P) Live*
678 *spermatocytes expressing endogenous EYFP tagged Rab proteins were incubated with PlyA2-*
679 *mCherry for one hour followed by washes with M3 insect media (2x) and imaged using spinning*
680 *disk confocal microscopy. (E-G) EYFP-Rab4 spermatocytes, (H-J) EYFP-Rab6 spermatocytes,*
681 *(K-M) EYFP-Rab7 spermatocytes, (N-P) EYFP-Rab11 spermatocytes. Arrowheads indicate*
682 *colocalizing structures. (Q) Colocalization coefficient (Mander's Coefficient) measurements*
683 *showing fraction of EYFP Rab proteins colocalize with internalized PlyA2-mCherry. Mander's*
684 *coefficient was determined using imageJ plugin JACoP. Each dot in the graph represents a 2D*

685 *image consisting of 8-16 spermatocytes, Rab4 (n=42), Rab6 (n=47), Rab7(n=36) and Rab11*
686 *(n=81). Statistical significance was calculated using mean, standard deviation (SD) and N in*
687 *Prism 9. The ordinary one-way Anova multiple comparison was used to calculate P values where*
688 *****P ≤ 0.0001;***P ≤ 0.001; **P ≤ 0.01; *P ≤ 0.05 and ns P >0.05.*

689 ***Fig.6. CPE containing endosomes translocate to cleavage furrows during male meiotic***
690 ***cytokinesis.*** *(A-F) The EYFP-Rab7 expressing spermatocytes are treated with PlyA2-mCherry and*
691 *snapshots of spermatocytes undergoing meiosis I cytokinesis are shown. (A-C) Horizontal view of*
692 *one z slice is shown (D-F) Cross sectional view of a spermatocyte undergoing cytokinesis,*
693 *maximum intensity projection image was shown. (G-I) Localization of EYFP-Rab7 in intact cysts*
694 *where spermatocytes are encapsulated by cyst cells. Horizontal view of a single z slice is shown.*
695 *(J-O) EYFP-Rab11 expressing spermatocytes were treated with PlyA2-mCherry and meiosis I*
696 *cytokinesis was imaged (J-L) Horizontal view of single z slice is shown. (M-O) Cross sectional*
697 *view, maximum intensity projection image is shown. White arrows indicate colocalization and*
698 *white arrowheads indicate lack of colocalization.*

699 ***Fig.S7. Cytological analysis of Rab11 and Rab7 mutants for meiotic cytokinesis defects.*** *(A)*
700 *Measurement of cytokinetic defects in testes squash preparations of wild type samples, 7*
701 *independent experiments and total round spermatid count of about (n=6000). (B) cytokinesis*
702 *defects in Rab11 dominant negative expressing gonads at 4th day, 5 independent experiments and*
703 *total round spermatid count of about (n=1500). Fraction of round spermatids showing nucleus to*
704 *mitochondria ratio 2:1 (2nucleus), 3:1 (3nucleus), 4:1 (4 nucleus) and 4 irregularly sized nucleus*
705 *with one mitochondrion are depicted. (c) Western blotting of protein extracts from control and*
706 *Rab7 mutants using Rab7 and Tubulin (loading control) antibodies. Lanes 1-4 (control), lanes 5-*
707 *8 (Rab7 mutants). (D) Fraction of cytokinetic defects in Rab7 null mutant pupal gonads (24-48*

708 *hours post pupation), 11 independent experiments and round spermatid count of about (n=1100).*
709 *(E) Comparison of total cytokinetic defects between Rab11DN and Rab7 mutants (sum of all forms*
710 *of cytokinetic defects including nuclear to mitochondria ratios 2:1, 3:1,4:1 and irregularly seized*
711 *nucleus). Each dot in each graph represents an independent experiment (n) that consisted of 10*
712 *individual testis/gonads.*

713 **Multivesicular bodies deliver CPE laden vesicles to the cleavage furrow**

714 We performed correlative light and focused ion beam scanning electron microscopy (CLEM/FIB-
715 SEM) to gain structural insight into the endosomes that are enriched at the cleavage
716 furrow/midbody during cytokinesis. Spermatocytes expressing EYFP-Rab7 were labeled for
717 endocytosed CPE with PlyA2-mCherry and allowed to progress to meiosis 1. Cysts showing
718 PlyA2-mCherry and EYFP-Rab7 co-localization at the cytokinetic furrow were fixed, imaged by
719 light microscopy, then stained, resin embedded and prepared for FIB-SEM. Figure 7A-C shows
720 CLEM-FIB-SEM of a cyst undergoing cytokinesis showing colocalization of Rab7 with
721 endocytosed CPE at the furrow. 3D correlation of the LM and FIB-SEM image volumes allowed
722 us to localize the Rab7/PlyA2 double positive signals to endosomes that appeared as spherical
723 shaped structures that ranged from 300 to 800 nm in diameter. The lumen of these endosomes was
724 filled with intraluminal material which at FIB-SEM resolutions could be discerned, but not
725 definitely resolved, as vesicles packed into the lumenal volume. Although we were able to capture
726 endosomes in the cytokinetic furrow it was technically difficult to visualize and arrest them in
727 physical association with the ingressing furrow membranes using these flies (Movie S14).
728 Therefore, we decided to examine cytokinesis in cysts where the contractile ring in proximity to
729 the ingressing membrane and the endosomes could be visualized during live imaging.

730 ***Fig.7. CPE positive endosomes dock at the ingressing cytokinetic furrow during meiosis***

731 *A. Combined transmitted and fluorescence image of dissected Drosophila cyst; dividing cells*
732 *chosen for FIB-SEM imaging are boxed. Green, eYFP-Rab7; Red, PlyA2-mCherry. Scale bar 20*
733 *µm. B. 2D section from FIB-SEM reconstruction correlated with "z slice" from confocal. Colors*
734 *as in A, saturated for ease of visualization. Scale bar 5 µm. C. Area boxed in B; FIB-SEM image*
735 *(top), Rab7 (middle), PlyA2 (bottom). Arrowheads indicate electron-dense endosomes. Scale bar*
736 *2 µm. D. Volumetric imaging of dividing spermatocytes, showing orthogonal imaging planes, and*
737 *expected cross sections for light microscopy (LM) and FIB-SEM. E. Fluorescence "z slice"*
738 *capturing a cleavage furrow in-plane. Scale bar 4 µm F. FIB-SEM image capturing same furrow*
739 *as in E cross-section, approximated by red lines. Scale bar 2 µm. G, H, I. Correlated fluorescence*
740 *image, overlay, and rotated FIB-SEM section, respectively, of furrow in-plane. J. Area boxed in I*
741 *showing endosomes docked at the furrow (arrow). Scale bar 1 µm. J. K. Volume rendering of*
742 *FIB-SEM 3D reconstruction, with furrow segmented and false colored red, undocked endosomes*
743 *green, docked endosomes blue. L. Close-up of K, with furrow segmented translucent and*
744 *endosomes unsegmented M. Matching FIB-SEM section in the imaging plane. Arrows in K, L, M*
745 *show same endosomes docked at furrow. Scale bar 2 µm. N. Independent CLEM/FIB-SEM*
746 *experiment revealing at higher pixel sampling another example of docked vesicle. Scale bar 1 µm.*
747 ***Fig. S8 Sample processing for FIB-SEM***
748 *A. Drosophila cysts were dissected onto a gridded cover slip, after fixation and embedment in 4%*
749 *agarose. The cyst of interest is circled and is the same as the cyst shown in Fig. 7A. B. Higher*
750 *magnification image of boxed area in A C. Light microscopy overview of full field before EM*
751 *processing D. Same field after EM processing. The same pattern of dissected cysts is visible,*
752 *suggesting spatial retention of sample. Trimmed area approximated with a dashed rectangle. E.*
753 *Field of view (orthogonal to Fig. 7A) with doubly labeled cleavage furrow of interest circled. F.*

754 *Sectioning at the microtome proceeded until furrow of interest was almost exposed (red circle).*
755 *FIB-SEM imaging was executed in the volume indicated by rectangle, in direction of arrow.*
756 We examined spermatocytes expressing tubulin-Gal4>mRFP-Anillin that labels the contractile
757 ring and endogenously expressing EYFP-Rab7 that marks late endosomes to capture membrane
758 proximal endosomes (Movie S15). Anillin (also known as scraps) encodes for a conserved
759 pleckstrin homology domain containing protein that was shown to bind actin, microtubules and
760 nonmuscle myosin II and required for stabilization of contractile ring [39]. Dividing cysts were
761 imaged, fixed and cysts with Rab7-Anilin colocalization at the cytokinetic furrow were prepared
762 for FIB-SEM imaging (Fig. 7D and E). Using CLEM/FIB-SEM we were able to capture multiple
763 Rab7 positive endosomes docked at the ingressing furrow (Fig. 7E-M). Movie S16 shows the 3D
764 reconstruction of the vesicles captured at the furrow seen in Fig. 7K. We observed multiple
765 instances of this docking of endosomes in dividing spermatocytes (Fig. 7N). Movie S17 is a sub-
766 volume reconstruction of the dividing cells seen in Figure 7N. While we observed docking of the
767 endosomes to the ingressing membrane in the samples we studied, we were unable to visualize the
768 fusion of vesicles to these ingressing membrane or to the proteinaceous structure that was
769 anchoring the endosomes (Fig. 7 and Movie S17). To visualize the endosomes at the furrow at
770 higher resolution, we carried out CLEM-SEM-TEM of the dividing meiotic spermatocytes and
771 examined vesicles that appeared to be in close proximity to the cleavage furrow (Fig.8).
772 *Drosophila* spermatocyte cysts expressing tubulin-Gal4>mRFP-Anillin and EYFP-Rab7
773 undergoing meiotic cytokinesis were identified, fixed and resin embedded. Serial sectioning of the
774 correlated cysts followed by TEM imaging revealed the structures as multivesicular body like
775 organelles, filled with intraluminal vesicles varying in size between 20-50 nm in diameter (Fig. 8C
776 and D), consistent with previously described multivesicular endosomes (MVEs) or Multivesicular

777 bodies (MVBs) [57]. Again, rather than seeing evidence of fusion, we found that outer membrane
778 of several of these endosomes was discontinuous (Fig.8C). Interestingly, the MVBs that showed
779 significant loss of outer membrane integrity appeared to have released intraluminal vesicles in the
780 vicinity of the ingressing membranes (Fig. 8D, top left), possibly providing a proximal source of
781 lipid laden vesicles for membrane biogenesis (Fig. 8E).

782 ***Fig.8. Multivesicular bodies release intraluminal vesicles at the cytokinetic furrow***

783 *A. Fluorescence maximum projection image capturing dividing cells from a dissected drosophila*
784 *cyst. Green, eYFP-Rab7; Red, mRFP-Anillin. Inset, vesicles adjacent to a cleavage furrow. Scale*
785 *bar 10 µm. B. Corresponding TEM section. Endosomes adjacent to the cleavage furrow are boxed.*
786 *Scale bar 10 µm. C. Higher magnification TEM image of area boxed in B. Scale bar 500 nm.*
787 *Arrows indicate discontinuity in outer membranes of MVBs. D. Subsequent TEM section of same*
788 *area, showing make-up of vesicles at high magnification. Scale bar 300 nm. E. A model depicting*
789 *endocytosis of CPE from plasma membrane, the maturation of these endosomes into multivesicular*
790 *bodies, targeting and release of intraluminal vesicles at the cleavage furrow.*

791 **Discussion**

792 Plasma membrane expansion and ingression of the cytokinetic furrow still remain one of the least
793 understood horizons in the field of cell division [58]. We are only beginning to appreciate the
794 involvement of lipids in structural integrity, membrane expansion, and transmission of signals
795 during cytokinesis. PIP2 is the most studied lipid in cytokinesis and has been shown to localize to
796 the cleavage furrow during ingression. In addition to PIP2, cholesterol, very long chain fatty acids
797 and sphingolipids have also been associated with cytokinesis [59] [10, 12]. In mitotic HeLa cells,
798 PIP2 accumulation at the inner leaflet and subsequent recruitment of RhoGTPase (RhoA) was
799 shown to be coordinated with sphingomyelin rich domains on the outer leaflet [10]. However, it

800 is unknown if a similar mechanism exists in germ cells which have different characteristics and
801 different lipid composition. While mitotic cells were shown to accumulate classical sphingolipids
802 with long to very long acyl chains at intercellular bridges [12], male germ cells accumulated
803 complex sphingolipids with very long/ultra long chain polyunsaturared fatty acids (VLC-PUFAs)
804 [13]. These differences in sphingolipid composition with distinct biophysical properties between
805 mitotic cells and male meiotic cells point towards existence of distinct underlying mechanisms.
806 In this study, we show the sphingolipid composition of the major species in *Drosophila* testis for
807 the first time and demonstrate significant enrichment of unique CPE species containing
808 SPH_MUFA and SPD_SFA. Unlike mammalian testis, the *Drosophila* testis lacks significant
809 amounts of VLC-PUFA containing sphingolipids. However, due to conserved unsaturation in acyl
810 chains, it is likely that SPH_MUFA and SPD_SFA containing CPE could substitute for VLC-
811 PUFA functions in *Drosophila* male germ cells. Glycosphingolipids with VLC/ULC PUFAs have
812 been shown to be required for mammalian male meiotic cytokinesis but their actual role has not
813 been delineated [13, 60, 61]. It is interesting to note that CPE mimics certain physical properties
814 of galactosylceramide (GalCer) a major sphingolipid in myelin sheath [62]. Previous studies have
815 shown that CPE has an essential role in axonal ensheathment and cortex glial plasma membrane
816 expansion in *Drosophila* [15, 63]. It was hypothesized that the axonal ensheathment in mammals
817 and *Drosophila* is based on similar physical process with different lipids [62]. We have previously
818 shown that sphingomyelin, a structural analog of CPE, could rescue cortex glial membrane defects
819 in *cpes* mutants suggesting the head group is not as important as the tail in glial membranes.
820 However, here we show that sphingomyelin could not rescue spermatogenesis defects in *cpes*
821 mutants alluding to the importance of the ethanolamine head group in spermatocytes. Taken
822 together, we could suggest that *Drosophila* CPE would have evolved to have both the properties

823 of mammalian glycosphingolipids and sphingomyelin to promote spermatogenesis and glial
824 ensheathment of neurons.
825 Phosphoinositides play critical role in cytokinesis. In particular, PIP2 was shown to be enriched at
826 the furrows and directly binds to several proteins such as anillin, septins and MgcRacGAP to
827 mediate furrow stability [64, 65]. Unlike mitotic cells, PIP2 in male meiotic cells does not show
828 selective accumulation at cleavage furrows. Instead, it is uniformly distributed throughout the
829 plasma membrane including at furrows ([45] and Fig.4C and Movie S5, S6 and S7). Interestingly,
830 PIP2 hydrolysis and calcium release were shown to be required for cytokinesis in *Drosophila*
831 spermatocytes [45]. These observations suggests that in meiotic cells, PIP2, has a broader role at
832 the plasma membrane and at furrows to promote cytokinesis. Intriguingly, we show that the PIP3
833 binding PH domain of Steppke (tGPH) localizes to cleavage furrows indicating a potential role for
834 PIP3 during male meiotic cytokinesis. However, the accumulation of PIP3 to the cleavage furrows
835 occurs only in the intact cysts i.e, 16 interconnected spermatocytes wrapped up by two somatic
836 cyst cells suggesting the need for certain mechanical force. The role of PIP3 accumulation in the
837 male meiotic cleavage furrows is an open question and warrants future investigation. Notably,
838 recently it was shown that cytohesin Steppke reduces tissue tension by inhibiting the actomyosin
839 activity at adherens junctions in embryos [46]. Although broad accumulation of PIP2 to the plasma
840 membranes and PIP3 accumulation at the cleavage furrows was not altered in *cpes* mutants, their
841 specific localization to membrane microdomains and their inability to signal robustly cannot be
842 ruled out. Sphingadienes with $\Delta^{4,6}$ conjugated double bonds were previously identified in
843 *Drosophila*, *Manduca sexta*, and *Bombyx mori* [66-68], although their enrichment in the testis was
844 not known until now. However, normal sphingolipid synthesis and their degradation are shown to
845 be required for spermatogenesis [69, 70]. The sphingadiene sphingolipids were shown to have

846 inhibitory effects on AKT-dependent signaling [71] and downregulate *Wnt* signaling via a
847 PP2A/Akt/GSK3β pathway [72]. Thus, accumulation of sphingadiene with saturated fatty acid
848 containing sphingolipids in the testis could have a role in regulation of PIP2/PIP3 mediated
849 signaling *in vivo*. Apart from CPE_SPD_SFA the *Drosophila* testis is also enriched in
850 CPE_SPH_MUFA suggesting they could mediate distinct functions. Lipids with unsaturated fatty
851 acids mediate a number of biological functions [73]. It is widely known that phospholipids with
852 unsaturated fatty acids promote membrane fluidity and elasticity [74, 75]. Sphingolipids with
853 unsaturated fatty acids could thus provide unique biophysical properties necessary for the
854 membrane curvature requirements during meiotic cytokinesis. *des-1* codes for dihdryoceramide
855 desaturase enzyme in the *de novo* biosynthetic pathway in *Drosophila*. *des-1* mutants (also called
856 *infertile crescent*, *ifc*) were described before the gene product was identified as a homolog of
857 dihydroceramide desaturase. The primary spermatocytes of the *des-1* mutants undergo
858 degeneration without initiating chromosome condensation at the beginning of meiosis [76]. A P-
859 element insertion allele showed that DES-1 colocalized with mitochondria and was intimately
860 associated with the central spindle of dividing meiotic spermatocytes. Its deficiency leads to failure
861 of central spindle assembly in these dividing cells leading to several phenotypes including
862 cytokinetic defects. It was proposed that DES-1 could be part of an anchoring mechanism that
863 linked membrane bound cellular compartments to components of the cytoskeleton [69].
864 Considering that DES-1 is a dihydroceramide desaturase homolog, it would be worth revisiting
865 the mutant phenotype to evaluate if it too contributes to membrane assembly at the cytokinetic
866 furrow due to lack of CPEs.
867 In correlative live imaging and electron microscopy studies, we find that multivesicular bodies
868 (MVBs) target CPE laden vesicles to the cleavage furrow. MVBs are by definition spherical

869 organelles that are typically 250-1000 nm in diameter with a single outer membrane that enclose
870 a variable number of smaller spherical vesicles within. Originally they were believed to be
871 involved in neurosecretion because of their close association with the Golgi stacks [77]. Further
872 work established a primary role in endocytosis and subsequent degradation of proteins [78-80].
873 Other work have highlighted the important role of MVBs in recycling function [81]. The last
874 decade or so has seen the emergence of a role for MVBs in autophagy, and secretion via the
875 exosomes [82, 83]. Our work has surprisingly unraveled a possible new function for MVBs in
876 transporting the endocytosed vesicles rich in lipids to the vicinity of expanding membrane.
877 Interestingly, CPE is not required for localization of MVBs to the cleavage furrow (Movie S18),
878 instead, our data suggests that CPE loaded MVBs are required in the vicinity of expanding
879 membranes to mediate cytokinesis. Future studies should throw light on the role of this pathway
880 in membrane and protein accumulation in newly synthesized membranes as in the case of meiotic
881 cytokinesis in the testis. The human genome encodes more than 60 Rab proteins and several of
882 them including Rab1, Rab8, Rab10, Rab14, Rab21, Rab24 and Rab35 were shown to localize to
883 intercellular bridges. However, most of the studies primarily focused on the recycling role of
884 Rab11 and Rab35 endosomes and their effector proteins in cytokinesis [65]. Currently it is
885 unknown if these endosomes are also involved in delivery of specific plasma membrane derived
886 lipids to the cleavage furrows. Our study shows that there is an increased localization of CPE to
887 the endosomal compartments in spermatocytes. The CPE containing MVBs are selectively docked
888 on the ingressing membranes at the cytokinetic furrow and release intraluminal vesicles,
889 suggesting delivery of CPE rich membranes to the growing furrows. Future investigations focusing
890 on these CPE enriched endosomes and their dyamics during male meiotic cytokinesis, spermatid

polarity and individualization will provide novel insights into membrane expansion and or their role as a signaling center to mediate spermatogenesis.

Materials and Methods

Fly stocks

tubulin-Gal4 (BDSC#5138), UAS-PLCδ-PH-EGFP (BDSC#39693), tGPH (BDSC#8163), Sqh-GFP.RLC (BDSC#57145), Sqh-mCherry.M (BDSC#59024), p(Ubi-p63E-Feo-mCherry)3 (BDSC#59277), *bam*-Gal4 [37], *nos*-Gal4 (BDSC#4937), *chif*-Gal4 (BDSC#13134), C587-Gal4 (BDSC#67747), EYFP-Rab4 (BDSC#62542), EYFP-Rab6 (BDSC#62544), EYFP-Rab7 (BDSC#62545), EYFP-Rab11(BDSC#62549), UAS-EGFP (BDSC#5430), tub-Gal80ts (BDSC#7108), UASP-Rab11.S25N (BDSC#23261), UAS-mRFP-Anillin (BDSC#52220), rab7 mutant (Krisztina Hegedus et al., 2016), genomic CPES_V5tag [15], *cpes* mutants [15], UAS-hSMS1 [15], dcert1[31], UAS CDase [32], UAS-CPES active site mutants, UAS-Aedes CPES, UAS-Bombyx CPES (this study).

Fly husbandry

All *Drosophila* stocks were raised on standard fly food and maintained 25°C unless otherwise mentioned. Due to increased lethality *cpes* mutants were raised at 18-21°C. Certain genetic backgrounds increased pupal death in *cpes* mutants such as overexpression of UAS CDase, UAS-PLCδ-PH-EGFP, *cpes*;*dcert*^{1} double mutants. In such cases we have separated 3rd instar larvae of *cpes* mutants and allowed them to develop into pupae. The testes were dissected before the death of pupae and analyzed.

914 **Cloning of UAS-*Aedes egypty* CPES and UAS-*Bombyx Mori* CPES**

915 The coding sequence for *Aedes aegypti* CPES (XM_021851518.1), and *Bombyx mori* CPES
916 (XM_004923146.3) were codon optimized and synthesized by GenScript® and subcloned into
917 pUAST vector. The clones were sent to BestGene Inc for embryo injection service. The transgenic
918 flies were balanced and crossed with Gal4 drivers to conduct rescue experiments.

919 **Cloning of CPES active site mutant**

920 Two conserved aspartates in CPES active site were mutated to alanine using PCR based site
921 directed mutagenesis method as described by [84]. PCR was performed using pBluescript SK+
922 CPES_V5 clone as template with appropriate sense and antisense primers (Table S1) and Phusion
923 polymerase (NEB). The PCR product was digested with DpnI to remove templates followed by
924 transformation into DH5α competent cells. Plasmids were isolated from colonies grown in LB
925 media and screened by restriction digestion with appropriate restriction enzymes (Table S1) and
926 sequencing. The pBluescript SK+ CPES DD-AA clone was used as template to PCR amplify the
927 insert using appropriate primers (Table S1), restriction digested and cloned into pUAST vector.
928 The clones were confirmed with restriction digestion followed by DNA sequencing.

929 **Cloning, expression, and purification of PlyA2mCherry**

930 Mushroom-derived aegerolysin PlyA2 was cloned, expressed, and purified as described by [85].
931 Briefly, the coding sequence of PlyA2 (accession number AB777517) fused to mCherry at the C-
932 terminus was synthesized by GenScript®. The linker amino acid sequence between PlyA2 and
933 mCherry was VDGTAGPGSIAT. This clone was used as template to PCR amplify using
934 appropriate forward and reverse primers (Table S1) and cloned into p24a vector at appropriate
935 restriction sites (Table S1). The clones were transformed into Escherichia coli strain BL-21 (DE3)
936 and single colony was inoculated in to 5ml of LB broth containing 50μg/ml kanamycin and grown

937 overnight in orbital shaker (200rpm) at 37°C. 2ml of overnight culture was inoculated into 250ml
938 of fresh LB broth containing kanamycin and grown at 37°C until the optical density reached to
939 0.6. Subsequently, the culture was incubated in cold (4°C) for 2 hours, followed by induction with
940 0.3mM isopropyl-B-D-thiogalactopyranoside and grown at 25°C in orbital shaker (200rpm)
941 overnight. The cells were harvested by centrifugation at 5,000g for 10min at 4°C and the pellet
942 was resuspended in binding buffer (20mM sodium phosphate buffer (pH 7.4), 500mM NaCl,
943 20mM imidazole) containing EDTA free protease inhibitor cocktail (Sigma, P8340). The cell
944 suspension (50 ml) was sonicated at 4°C (Cole-Parmer ultrasonic processor model CP130,) with
945 microprobe at an amplitude of 30 and on and off cycles of 10sec each for about 30 min to 1 hour.
946 The lysate was centrifuged at 10,000g for 10min to remove insoluble proteins and debris. To the
947 supernatant, 1ml of 50% Ni-NTA agarose (Thermo Scientific) was added and incubated on end-
948 to-end rotor for 3 hours and the beads were collected on a column and washed with 30ml of binding
949 buffer and eluted with binding buffer containing 200mM imidazole. The fractions were dialysed
950 in 20mM sodium phosphate buffer 3 times (1L each) and the final protein was concentrated with
951 Amicon centriprep filter devices for volumes up to 15ml. The protein concentration was
952 determined using Bradford assay. The proteins were resuspended in 20% glycerol, aliquoted
953 (100µl) and stored at -80°C for future use.

954 **Testis squash preparation, phase contrast microscopy, and immunofluorescence microsocpy**

955 *Drosophila* testis squash preparations for phase-contrast microscopy and immunostaining were
956 performed as described by [17]. Briefly, young male (0-2 days old) testis were dissected (5 pairs)
957 in phosphate-buffered saline (PBS, 130 mM NaCl, 7mM Na2HPO4, 3mMH2PO4). The testes
958 were torn open on a slide at appropriate location with a pair of Black Anodized Steel needles (tip
959 diameter 0.0175mm) and a cover glass was gently placed without air bubbles. The slides were

960 directly observed under phase-contrast microscopy or snap frozen in liquid nitrogen for
961 immunostaining. After freezing the cover glass was removed from the slide with razor blade and
962 immersed in cold 99.5% ethanol and incubated in -20°C for 10 min. The slides were then fixed
963 with 4% paraformaldehyde (PFA) in PBS containing 0.1% Triton-X-100 (PBST) for 15 min.
964 Subsequently, the slides were washed with PBS and the area of squashed tissue was circled with a
965 hydrophobic barrier pen, permeabilized with PBST (30 min) and blocked with 5% normal goat
966 serum in PBST (1 hour at RT). Squashed tissues were incubated with primary (1μg in 100μl) and
967 secondary antibody (1:100 dilution) (8-12 hours each at 4°C in a moist chamber). Slides were
968 washed with PBST (3x 10 min each) after each antibody treatment, finally incubated with DAPI
969 solution (1:2000 dilution from 5mg/ml stock, Molecular Probes) and mounted with Vectashield
970 H1000 mounting media.

971 **Quantification of cytokinetic defects**

972 5 pairs of testes were dissected for each experiment, live testis squashes were prepared and round
973 spermatids were observed using 40X Ph2 Plan-Neofluar objectives on Axioplan 2 microscope as
974 described above. All round spermatid cyst in the sample were imaged and their cell number was
975 counted manually (250-500) for each genotype. Percentage of round spermatids with 2, 3 or 4
976 nuclei were calculated by dividing the with total spermatid number including spermatids with 1,
977 2, 3, or 4 nuclei. More than 5 independent experiments were carried out for each genotype.

978 **Male fertility assay**

979 Male fertility assay was performed by setting up individual crosses with 1 male and 3 wild type
980 females. Each replicate involved 30 males and three independent replicates (total of 90 males)
981 were performed for each experiment.

982

983 **Immunostaining and confocal imaging**

984 *Drosophila* tissues were dissected and immunostained as described previously [15]. Briefly,
985 dissected testes were fixed with 4% PFA in 0.3% PBST for 1 hours at RT, washed (3x 10 min
986 each), permeabilized in 0.3% PBST (1 hour), blocked with 5% NGS (1hour) and incubated with
987 primary antibody (1:100 dilution or 1µg in 100µl of 5% NGS in PBST) overnight (8-12 hours).
988 Testes were washed with 0.3% PBST (3x10min each) and incubated with secondary antibody
989 (1:100 dilution in 5%NGS in PBST). Testes were washed with PBST (3x 10 min each), stained
990 with DAPI (1:2000 dilution of 5mg/ml solution in PBST) for 15 min, and mounted with
991 Vectashield H1000 mounting medium. The slides were imaged on ZEISS confocal laser scanning
992 microscope LSM 780 or LSM880.

993 **Live cell imaging of meiotic cysts**

994 About 15-20 pairs of young (0-2days old) *Drosophila* testes were dissected in 600µl of insect cell
995 culture media (M3 media supplemented with heat inactivated FBS, Pen/Strep) in a glass well plate.
996 Testes were transferred to a fresh well with 400µl of media and torn open with a pair of Black
997 Anodized Steel needles (tip diameter 0.01mm) to release the cysts into media. This was repeated
998 until all the testes were torn open. They were gently agitated so that all the cysts were released into
999 the media followed by removal of empty testis or debris from the media. The cysts were gently
1000 washed with fresh 400µl media (2x), then transferred *via* pipetting into the middle of 35mm cover
1001 glass bottom dish (Poly D-Lysine coated) and fresh media (max. 200µl) was gently added to the
1002 cleft formed between cover glass and the dish. The cysts tend to move while handling but remain
1003 settled on the cover glass and ideally remain in position while imaging. The intact cysts and cysts
1004 that have lost their cyst cells could be distinguished in brightfield view. The cysts that are
1005 beginning to undergo meiosis could be identified in brightfield view by looking at cell morphology

1006 and differences in nucleus and spindle appearance. Cells beginning to undergo meiosis could also
1007 be identified by Feo-mCherry which is localized to nucleus in interphase but translocates to cytosol
1008 during prophase to anaphase. Prophase to anaphase cysts were identified using 25x water objective
1009 and subsequently imaged using 63x water objective on a Leica Andor spinning disk confocal
1010 microscope. The time lapse imaging was done at 2 min intervals with the z stacks (about 80 slices,
1011 0.5µm per slice) at each time point for 60 to 90 min for completion of meiotic I cytokinesis. Laser
1012 power and exposure times were preferably kept low to prevent bleaching and aberrant effects on
1013 cytokinesis due to generation of free radicals.

1014 **Sample preparation for correlative light and electron microscopy (CLEM)**

1015 About 10-15 pairs of testes were dissected from newly eclosed male flies in M3 or S2 insect cell
1016 culture media. Testes were transferred to fresh M3 media (400 µl) in a Glass Spot plate (PYREX
1017 722085) and torn open with a pair of black anodized steel needles and gently agitated to release
1018 the cysts into media. Subsequently, testis debris were removed from the well. The cysts were gently
1019 washed with fresh 400 µl media (2x) and incubated with PlyA2-mCherry protein (10µg /ml) in
1020 400µl of M3 media for 1 hour, on a rocker. The cysts were washed with fresh media without
1021 PlyA2-mCherry (1x with 400µl media). About 5-10 cysts were transferred to cover glass bottom
1022 96 well plate (Cellvis, Cat # P96-0-N) containing 100µl of M3 media. The cysts in each well were
1023 observed under 25X water objective on an Andor spinning disk microscope using bright field and
1024 or fluorescence. Cells undergoing division were identified by cell morphology changes such as
1025 cell rounding, nuclear membrane loss, microtubule appearance, cell elongation and ingressing
1026 cleavage furrows. When spermatocytes at the appropriate stage of interest were identified, 100 µl
1027 of 8% PFA in M3 media was added to the well (4% PFA final concentration) and gently mixed
1028 with pipetting. The 96 well plate cover was removed after adding PFA to avoid its effect on other

1029 wells. Location of the well could be identified with the help of a torch light and or illuminating the
1030 well with bright field or fluorescent light. The process was repeated until at least 5-10 cysts were
1031 identified, and fixed. The sample in fixative could be stored up to 2 days at 4ºC in the 96 well
1032 plate. The cysts in the 96 well plate were gently agitated with pipetting and transferred to a glass
1033 spot plate (the pipet tip was cut and conditioned with the media to avoid sticking of cysts to tip
1034 walls). At this stage cysts were pooled from different 96 plate wells into a single glass well plate.
1035 The cysts were centered by gently flushing with pipetting. They were then washed with 1XPBS
1036 (3X 400 µl). Following washing, the cysts were pipetted into the center of a gridded covered glass
1037 bottom plate (MatTek, Part No. P35G-1.5-14-C-Grid). After the cysts settled on the coverslip,
1038 most of the PBS was removed by gentle pipetting. Subsequently 4% low melting agarose
1039 (Invitrogen, REF 16520-100) (in 1xPBS) that was maintained at 80 ºC is cooled for 1-2 min and
1040 gently poured from the top, care must be taken to minimize movement of cysts. After the agarose
1041 had solidified, the cysts that were settled and embedded in the agarose were imaged on the Andor
1042 spinning disk confocal microscope using 25X and 63X water objectives. At this time, the cells
1043 were imaged at high magnification by transmitted light to record the location of regions of interest
1044 (ROI) with respect to the alphanumeric grid of the glass-bottom dish. Images were also taken at
1045 lower magnification to record the locations of other cells in the dish, which would later serve as
1046 landmarks in the correlative light-electron microscopy (CLEM) pipeline; images of the ROI at
1047 various points in this pipeline are shown in Fig.S8.
1048 The disc of solidified agarose containing the cysts was carefully removed from the glass-bottom
1049 dish. Not only are the cells embedded in situ typically within 10 microns of the bottom agarose
1050 surface, but the alphanumeric gridded pattern is also transferred to the agarose pad in relief, and
1051 both are visible in a dissection microscope. The agarose pad was rinsed with 0.1 M sodium

1052 cacodylate buffer (11652, Electron Microscopy Sciences) several times. It was then incubated in
1053 a solution containing 2% osmium tetroxide (19150, Electron Microscopy Sciences) and 1.5%
1054 potassium ferricyanide (20150, Electron Microscopy Sciences) in 0.1M sodium cacodylate buffer
1055 for 1 hour at room temperature. Afterwards, it was thoroughly washed with water for a minimum
1056 of 30 minutes. The sample was then incubated in 1% aqueous uranyl acetate (22400, Electron
1057 Microscopy Sciences) for 30 minutes followed by extensive water washes. This was followed by
1058 standard EM processing steps – the sample was dehydrated using a series of increasing ethanol
1059 concentrations ending in 100% ethanol, and then washed with 100% propylene oxide. The sample
1060 was infiltrated with Epon (Embed 812) resin using increasing concentrations of hard resin
1061 formulation in propylene oxide, and finally embedment in a polypropylene dish, with curing in an
1062 oven at 60C for 2 days. Once the resin was fully cured, it was separated from the dish and examined
1063 using a dissecting microscope. The heavy metal-stained cysts were dark and easily identified; the
1064 overall pattern of cysts was unchanged from previous steps (Fig.S8). ROIs for CLEM were
1065 identified and ~1 mm^2 areas around each cyst were cut out from the larger disc of resin using a
1066 saw and razor blades. These were then re-embedded onto blank blocks for ultramicrotomy. The
1067 blocks were sectioned using an ultramicrotome (Powertome, RMC) until cysts were exposed at
1068 the resin surface as revealed by Toluidine Blue stain, taking care that the actual cleavage furrow
1069 itself was just below the surface and not sectioned. This positions the feature within ~10 microns
1070 of the top surface and therefore amenable to FIB-SEM imaging.

1071 **FIB-SEM, STEM and TEM imaging**

1072 FIB-SEM imaging was done largely as previously described [86]. Briefly, the specimen was cut
1073 to ~ 2mm height and mounted on a SEM stub using silver. The specimen was introduced into a
1074 Zeiss CrossBeam 550 (Zeiss Inc.), ROI located by SEM imaging, and protected by a patterned

1075 platinum and carbon pad. A trench was FIB milled until the profiles of both dividing cells were
1076 revealed but stopped before the cleavage furrow was milled away. Images were acquired at 3 nm
1077 or 5 nm pixel sampling in XY, and step size of 9 or 15 nm in Z, respectively, in an automated FIB-
1078 mill-SEM-image cycle with SEM operated at 1.5 kV, 1.2 nA; FIB milling at 30 kV, 1.5 nA, and
1079 back-scatter detector grid voltage at 900 V. The image stack was registered, contrast inverted and
1080 binned by 3 in the imaging plane to produce an isotropic 9 nm^3 or 15 nm^3 image volume
1081 reconstruction. For TEM imaging, the cysts were exposed using the same approach, but here, 60
1082 nm serial sections were cut and collected onto TEM grids. STEM imaging was executed at a Zeiss
1083 Gemini II SEM 450 at 30 kV landing energy, and the TEM imaging was done on a Hitachi 1050
1084 operated at 80 kV. In both cases, the grids were not post-stained, however a ~4nm carbon coat was
1085 applied using a sputter coater (Leica Inc.) before imaging.

1086 **Image correlation and visualization**

1087 There were two stages of correlation in these experiments. The correlation for relocation, i.e.,
1088 imaging an ROI by LM and then locating the same ROI for EM, was performed by careful sample
1089 preparation and appropriate imaging at various stages (Supp Fig S1). Correlation for registration,
1090 i.e., aligning two image volumes to identify cellular features of interest, was done after LM and
1091 EM images were acquired. 3D correlation was done using eC-CLEM [87]. The confocal stack and
1092 FIB-SEM image stacks were imported, and multiple fiducials were placed at distributed locations
1093 on the plasma membrane of both dividing cells in the PlyA2-mCherry + eYFP-Rab7 expressing
1094 cysts. The plasma membrane was visualized easily in the FIB-SEM images, and more
1095 approximately in the lower resolution LM data, using the PlyA2-mCherry signal which localizes
1096 strongly at the cell membrane. The green channel (Rab7) was not used for registration. The skew
1097 transformed LM fluorescence was overlaid on the original FIB-SEM data and examined with the

1098 green channel added back, upon which the identity of the PlyA2 + Rab7 double positive features
1099 in the furrow were revealed (Supplementary Movie S14). In a second experiment using mRFP-
1100 Anillin:eYFP-Rab7 cysts (Fig. 7E), the correlation in ecCLEM was performed using fiducial
1101 points on the furrow, as located by the "neck" in the FIB-SEM image volume (Fig. 7F), and the
1102 mRFP-Anillin staining in the LM images (Fig. 7G). As before, the Rab7 signal was not used for
1103 correlation. In both cases, the registration was limited by the relatively lower resolution of the LM
1104 image stack but was sufficient to consistently correlate large vesicles in the FIB-SEM data with
1105 Rab7-positive signals in the LM data. For TEM imaging, sequential sections were imaged and
1106 inspected manually until the features captured in the LM started to appear in the EM sections. The
1107 images were overlaid but not computationally correlated, as the identity of the features was readily
1108 apparent in the 2D EM image. The FIB-SEM image volumes were visualized, and volume
1109 rendered using Arivis (Arivis Inc), with features of interest such as furrow, docked and undocked
1110 vesicles segmented either in 3DSlicer (www.slicer.org) or Arivis.

1111 **Sphingolipid estimation in fly tissues using supercritical fluid chromatography**
1112 **coupled to mass spectrometry (SFC/MS/MS)**

1113 Sphingolipid estimation using supercritical fluid chromatography coupled to mass spectrometry
1114 (SFC/MS/MS) was performed as described previously [15]. Lipids were extracted from heads,
1115 ovary and testis samples as described [88, 89]. About 400 fly heads, about 250 pairs of ovaries and
1116 about 250 pairs of testes were used for each biological replicate. Three independent replicates were
1117 taken for each sample. For Figs.1 and 2 only testes samples were used whereas for Fig.4 whole
1118 male organ (testis, accessory glands, collecting ducts and ejaculation bulb) were used for lipid
1119 extraction. Internal standards (ISTD) added to the tissues before extraction included 500 pmol (20
1120 µl) of Cer/Sph Mixture I (Avanti Polar Lipids LM-6002), and 1nmol of C12 Sphingosyl PE

1121 (C17:1/C12:0) (Avanti Polar Lipids). Lipids from all samples were normalized to carbon content
1122 (100µg/ml) and 100µg/ml sample was diluted 10 times before injection for SFC. We have used
1123 large-fragment MRM method for quantitation of amount per 100µg of carbon.

1124 **Total RNA sequencing**

1125 Three independent biological replicates were performed for each sample and about 200 pairs of
1126 w^{1118} (WT 1-3), *cpes* mutant (KO 1-3) and *bam*-Gal4>UAS-CPES rescued (RES 1-3) fly testis
1127 were dissected for each replicate. The testes were dissected in S2 cell culture media, washed with
1128 PBS and RNA was extracted. Total RNA was extracted using Trizol method followed by DNAase
1129 I treatment and purification using RNA Clean and Concentrator™-5 kit (Zymoresearch). A total
1130 of 2µg of RNA was submitted to Novogene for total RNA seq. The RNA seq data was further
1131 analyzed for differential gene expression and pathway analysis using Gene Set Enrichment
1132 Analysis (GSEA). The gene sets specific for *Drosophila* were downloaded from
1133 http://www.bioinformatics.org/go2msig/ and http://ge-lab.org/gskb/. The gene sets specific for cell
1134 types in *Drosophila* testis are described in Evan Witt et al., 2019 [33].

1135 **Acknowledgments**

1136 This study was funded by the intramural division of the National Cancer Institute, National
1137 Institutes of Health (Division of Health and Human Services). The content of this publication does
1138 not necessarily reflect the views or policies of the Department of Health and Human Services, nor
1139 does mention of trade names, commercial products, or organizations imply endorsement by the
1140 U.S. Government. The study was partly funded with Frederal funds from the National Cancer
1141 Institute, National Institutes of Health, under Contract No. 75N91019D00024. The work was
1142 partially supported by the Grant-in-Aid for Scientific Research on Innovative Areas (17H06304)
1143 [T.B.] and a Grant-in-Aid for Scientific Research (B) (18H01800) [T.B.] from Japan Society for

the Promotion of Science (JSPS). We thank Mr. Aayush Bhtawadekar for help with movies and rendering for the FIB-SEM images.

Conflict of Interest Statement

The authors declare no conflicts of interests.

References

1. Fahy E, Subramaniam S, Murphy RC, Nishijima M, Raetz CR, Shimizu T, et al. Update of the LIPID MAPS comprehensive classification system for lipids. J Lipid Res. 2009;50 Suppl:S9-14. Epub 2008/12/23. doi: 10.1194/jlr.R800095-JLR200. PubMed PMID: 19098281; PubMed Central PMCID: PMCPMC2674711.
2. Harayama T, Riezman H. Understanding the diversity of membrane lipid composition. Nat Rev Mol Cell Biol. 2018;19(5):281-96. Epub 2018/02/08. doi: 10.1038/nrm.2017.138. PubMed PMID: 29410529.
3. Kutateladze TG. Translation of the phosphoinositide code by PI effectors. Nat Chem Biol. 2010;6(7):507-13. Epub 2010/06/19. doi: 10.1038/nchembio.390. PubMed PMID: 20559318; PubMed Central PMCID: PMCPMC3182472.
4. Hunt AN, Skippen AJ, Koster G, Postle AD, Cockcroft S. Acyl chain-based molecular selectivity for HL60 cellular phosphatidylinositol and of phosphatidylcholine by phosphatidylinositol transfer protein alpha. Biochim Biophys Acta. 2004;1686(1-2):50-60. Epub 2004/11/04. doi: 10.1016/j.bbalip.2004.08.003. PubMed PMID: 15522822.
5. Shulga YV, Topham MK, Epand RM. Study of arachidonoyl specificity in two enzymes of the PI cycle. J Mol Biol. 2011;409(2):101-12. Epub 2011/04/12. doi: 10.1016/j.jmb.2011.03.071. PubMed PMID: 21477596; PubMed Central PMCID: PMCPMC3095698.
6. Schuhmacher M, Grasskamp AT, Barahtjan P, Wagner N, Lombardot B, Schuhmacher JS, et al. Live-cell lipid biochemistry reveals a role of diacylglycerol side-chain composition for cellular lipid dynamics and protein affinities. Proc Natl Acad Sci U S A. 2020;117(14):7729-38. Epub 2020/03/28. doi: 10.1073/pnas.1912684117. PubMed PMID: 32213584; PubMed Central PMCID: PMCPMC7149225.
7. Rodriguez-Gallardo S, Kurokawa K, Sabido-Bozo S, Cortes-Gomez A, Ikeda A, Zoni V, et al. Ceramide chain length-dependent protein sorting into selective endoplasmic reticulum exit sites. Sci Adv. 2020;6(50). Epub 2020/12/15. doi: 10.1126/sciadv.aba8237. PubMed PMID: 33310842; PubMed Central PMCID: PMCPMC7732199.
8. Contreras FX, Ernst AM, Haberkant P, Bjorkholm P, Lindahl E, Gonen B, et al. Molecular recognition of a single sphingolipid species by a protein's transmembrane domain. Nature. 2012;481(7382):525-9. Epub 2012/01/11. doi: 10.1038/nature10742. PubMed PMID: 22230960.
9. Li R. Cytokinesis in development and disease: variations on a common theme. Cell Mol Life Sci. 2007;64(23):3044-58. Epub 2007/09/21. doi: 10.1007/s00018-007-7285-6. PubMed PMID: 17882379.
10. Abe M, Makino A, Hullin-Matsuda F, Kamijo K, Ohno-Iwashita Y, Hanada K, et al. A role for sphingomyelin-rich lipid domains in the accumulation of phosphatidylinositol-4,5-bisphosphate

1183 to the cleavage furrow during cytokinesis. Mol Cell Biol. 2012;32(8):1396-407. Epub 2012/02/15.
1184 doi: 10.1128/MCB.06113-11. PubMed PMID: 22331463; PubMed Central PMCID:
1185 PMCPMC3318597.
1186 11. Atilla-Gokcumen GE, Bedigian AV, Sasse S, Eggert US. Inhibition of glycosphingolipid
1187 biosynthesis induces cytokinesis failure. J Am Chem Soc. 2011;133(26):10010-3. Epub
1188 2011/06/15. doi: 10.1021/ja202804b. PubMed PMID: 21668028; PubMed Central PMCID:
1189 PMCPMC3131740.
1190 12. Atilla-Gokcumen GE, Muro E, Relat-Goberna J, Sasse S, Bedigian A, Coughlin ML, et al.
1191 Dividing cells regulate their lipid composition and localization. Cell. 2014;156(3):428-39. Epub
1192 2014/01/28. doi: 10.1016/j.cell.2013.12.015. PubMed PMID: 24462247; PubMed Central PMCID:
1193 PMCPMC3909459.
1194 13. Rabionet M, Bayerle A, Jennemann R, Heid H, Fuchser J, Marsching C, et al. Male meiotic
1195 cytokinesis requires ceramide synthase 3-dependent sphingolipids with unique membrane
1196 anchors. Hum Mol Genet. 2015;24(17):4792-808. Epub 2015/06/06. doi: 10.1093/hmg/ddv204.
1197 PubMed PMID: 26045466.
1198 14. Robinson BS, Johnson DW, Poulos A. Novel molecular species of sphingomyelin containing
1199 2-hydroxylated polyenoic very-long-chain fatty acids in mammalian testes and spermatozoa. J
1200 Biol Chem. 1992;267(3):1746-51. Epub 1992/01/25. PubMed PMID: 1730716.
1201 15. Kunduri G, Turner-Evans D, Konya Y, Izumi Y, Nagashima K, Lockett S, et al. Defective
1202 cortex glia plasma membrane structure underlies light-induced epilepsy in cpes mutants. Proc
1203 Natl Acad Sci U S A. 2018;115(38):E8919-E28. Epub 20180905. doi: 10.1073/pnas.1808463115.
1204 PubMed PMID: 30185559; PubMed Central PMCID: PMCPMC6156639.
1205 16. Demarco RS, Eikenes AH, Haglund K, Jones DL. Investigating spermatogenesis in
1206 Drosophila melanogaster. Methods. 2014;68(1):218-27. Epub 20140502. doi:
1207 10.1016/j.ymeth.2014.04.020. PubMed PMID: 24798812; PubMed Central PMCID:
1208 PMCPMC4128239.
1209 17. Sitaram P, Hainline SG, Lee LA. Cytological analysis of spermatogenesis: live and fixed
1210 preparations of Drosophila testes. J Vis Exp. 2014;(83):e51058. Epub 2014/01/30. doi:
1211 10.3791/51058. PubMed PMID: 24473184; PubMed Central PMCID: PMCPMC4089415.
1212 18. Gonzalez C, Casal J, Ripoll P. Relationship between chromosome content and nuclear
1213 diameter in early spermatids of Drosophila melanogaster. Genet Res. 1989;54(3):205-12. Epub
1214 1989/12/01. doi: 10.1017/s0016672300028664. PubMed PMID: 2515989.
1215 19. Fuller MT. Spermatogenesis. In: Bate MaM-A, A., editor. The Development of Drosophila.
1216 Cold Spring Harbor, NY: Cold Spring Harbor Laboratory Press; 1993. p. 71-147.
1217 20. Basu J, Williams BC, Li Z, Williams EV, Goldberg ML. Depletion of a Drosophila homolog of
1218 yeast Sup35p disrupts spindle assembly, chromosome segregation, and cytokinesis during male
1219 meiosis. Cell Motil Cytoskeleton. 1998;39(4):286-302. Epub 1998/04/29. doi: 10.1002/(SICI)1097-
1220 0169(1998)39:4<286::AID-CM4>3.0.CO;2-1. PubMed PMID: 9556329.
1221 21. Carmena M, Riparbelli MG, Minestrini G, Tavares AM, Adams R, Callaini G, et al.
1222 Drosophila polo kinase is required for cytokinesis. J Cell Biol. 1998;143(3):659-71. Epub
1223 1998/11/13. doi: 10.1083/jcb.143.3.659. PubMed PMID: 9813088; PubMed Central PMCID:
1224 PMCPMC2148135.

1225 22. Castrillon DH, Wasserman SA. Diaphanous is required for cytokinesis in Drosophila and
1226 shares domains of similarity with the products of the limb deformity gene. Development.
1227 1994;120(12):3367-77. Epub 1994/12/01. PubMed PMID: 7821209.
1228 23. Giansanti MG, Bonaccorsi S, Williams B, Williams EV, Santolamazza C, Goldberg ML, et al.
1229 Cooperative interactions between the central spindle and the contractile ring during Drosophila
1230 cytokinesis. Genes Dev. 1998;12(3):396-410. Epub 1998/02/28. doi: 10.1101/gad.12.3.396.
1231 PubMed PMID: 9450933; PubMed Central PMCID: PMCPMC316479.
1232 24. Gunsalus KC, Bonaccorsi S, Williams E, Verni F, Gatti M, Goldberg ML. Mutations in
1233 twinstar, a Drosophila gene encoding a cofilin/ADF homologue, result in defects in centrosome
1234 migration and cytokinesis. J Cell Biol. 1995;131(5):1243-59. Epub 1995/12/01. doi:
1235 10.1083/jcb.131.5.1243. PubMed PMID: 8522587; PubMed Central PMCID: PMCPMC2120640.
1236 25. Williams BC, Riedy MF, Williams EV, Gatti M, Goldberg ML. The Drosophila kinesin-like
1237 protein KLP3A is a midbody component required for central spindle assembly and initiation of
1238 cytokinesis. J Cell Biol. 1995;129(3):709-23. Epub 1995/05/01. doi: 10.1083/jcb.129.3.709.
1239 PubMed PMID: 7730406; PubMed Central PMCID: PMCPMC2120429.
1240 26. Steinhauer J. Separating from the pack: Molecular mechanisms of Drosophila spermatid
1241 individualization. Spermatogenesis. 2015;5(2):e1041345. Epub 2015/09/29. doi:
1242 10.1080/21565562.2015.1041345. PubMed PMID: 26413413; PubMed Central PMCID:
1243 PMCPMC4581072.
1244 27. Arama E, Agapite J, Steller H. Caspase activity and a specific cytochrome C are required
1245 for sperm differentiation in Drosophila. Dev Cell. 2003;4(5):687-97. Epub 2003/05/10. doi:
1246 10.1016/s1534-5807(03)00120-5. PubMed PMID: 12737804.
1247 28. Vacaru AM, van den Dikkenberg J, Ternes P, Holthuis JC. Ceramide phosphoethanolamine
1248 biosynthesis in Drosophila is mediated by a unique ethanolamine phosphotransferase in the Golgi
1249 lumen. J Biol Chem. 2013;288(16):11520-30. Epub 2013/03/02. doi: 10.1074/jbc.M113.460972.
1250 PubMed PMID: 23449981; PubMed Central PMCID: PMCPMC3630839.
1251 29. Henneberry AL, Wright MM, McMaster CR. The major sites of cellular phospholipid
1252 synthesis and molecular determinants of Fatty Acid and lipid head group specificity. Mol Biol Cell.
1253 2002;13(9):3148-61. Epub 2002/09/11. doi: 10.1091/mbc.01-11-0540. PubMed PMID:
1254 12221122; PubMed Central PMCID: PMCPMC124149.
1255 30. Williams JG, McMaster CR. Scanning alanine mutagenesis of the CDP-alcohol
1256 phosphotransferase motif of Saccharomyces cerevisiae cholinephosphotransferase. J Biol Chem.
1257 1998;273(22):13482-7. Epub 1998/06/05. doi: 10.1074/jbc.273.22.13482. PubMed PMID:
1258 9593682.
1259 31. Rao RP, Yuan C, Allegood JC, Rawat SS, Edwards MB, Wang X, et al. Ceramide transfer
1260 protein function is essential for normal oxidative stress response and lifespan. Proc Natl Acad Sci
1261 U S A. 2007;104(27):11364-9. Epub 2007/06/27. doi: 10.1073/pnas.0705049104. PubMed PMID:
1262 17592126; PubMed Central PMCID: PMCPMC1899189.
1263 32. Acharya U, Patel S, Koundakjian E, Nagashima K, Han X, Acharya JK. Modulating
1264 sphingolipid biosynthetic pathway rescues photoreceptor degeneration. Science.
1265 2003;299(5613):1740-3. Epub 2003/03/15. doi: 10.1126/science.1080549. PubMed PMID:
1266 12637747.
1267 33. Witt E, Benjamin S, Svetec N, Zhao L. Testis single-cell RNA-seq reveals the dynamics of
1268 de novo gene transcription and germline mutational bias in Drosophila. Elife. 2019;8. Epub

1269 20190816. doi: 10.7554/eLife.47138. PubMed PMID: 31418408; PubMed Central PMCID:
1270 PMCPMC6697446.
1271 34. Decotto E, Spradling AC. The Drosophila ovarian and testis stem cell niches: similar
1272 somatic stem cells and signals. Dev Cell. 2005;9(4):501-10. doi: 10.1016/j.devcel.2005.08.012.
1273 PubMed PMID: 16198292.
1274 35. Larkin A, Marygold SJ, Antonazzo G, Attrill H, Dos Santos G, Garapati PV, et al. FlyBase:
1275 updates to the Drosophila melanogaster knowledge base. Nucleic Acids Res. 2021;49(D1):D899-
1276 D907. doi: 10.1093/nar/gkaa1026. PubMed PMID: 33219682; PubMed Central PMCID:
1277 PMCPMC7779046.
1278 36. White-Cooper H. Tissue, cell type and stage-specific ectopic gene expression and RNAi
1279 induction in the Drosophila testis. Spermatogenesis. 2012;2(1):11-22. doi: 10.4161/spmg.19088.
1280 PubMed PMID: 22553486; PubMed Central PMCID: PMCPMC3341242.
1281 37. Chen D, McKearin DM. A discrete transcriptional silencer in the bam gene determines
1282 asymmetric division of the Drosophila germline stem cell. Development. 2003;130(6):1159-70.
1283 doi: 10.1242/dev.00325. PubMed PMID: 12571107.
1284 38. Bunt SM, Monk AC, Siddall NA, Johnston NL, Hime GR. GAL4 enhancer traps that can be
1285 used to drive gene expression in developing Drosophila spermatocytes. Genesis.
1286 2012;50(12):914-20. Epub 20120912. doi: 10.1002/dvg.22341. PubMed PMID: 22926963.
1287 39. Giansanti MG, Sechi S, Frappaolo A, Belloni G, Piergentili R. Cytokinesis in Drosophila male
1288 meiosis. Spermatogenesis. 2012;2(3):185-96. doi: 10.4161/spmg.21711. PubMed PMID:
1289 23094234; PubMed Central PMCID: PMCPMC3469441.
1290 40. Wang H, Brust-Mascher I, Scholey JM. The microtubule cross-linker Feo controls the
1291 midzone stability, motor composition, and elongation of the anaphase B spindle in Drosophila
1292 embryos. Mol Biol Cell. 2015;26(8):1452-62. Epub 2015/02/20. doi: 10.1091/mbc.E14-12-1631.
1293 PubMed PMID: 25694445; PubMed Central PMCID: PMCPMC4395126.
1294 41. Royou A, Field C, Sisson JC, Sullivan W, Karess R. Reassessing the role and dynamics of
1295 nonmuscle myosin II during furrow formation in early Drosophila embryos. Mol Biol Cell.
1296 2004;15(2):838-50. Epub 2003/12/06. doi: 10.1091/mbc.e03-06-0440. PubMed PMID:
1297 14657248; PubMed Central PMCID: PMCPMC329397.
1298 42. Brill JA, Wong R, Wilde A. Phosphoinositide function in cytokinesis. Curr Biol.
1299 2011;21(22):R930-4. Epub 2011/11/26. doi: 10.1016/j.cub.2011.10.001. PubMed PMID:
1300 22115464.
1301 43. Britton JS, Lockwood WK, Li L, Cohen SM, Edgar BA. Drosophila's insulin/PI3-kinase
1302 pathway coordinates cellular metabolism with nutritional conditions. Dev Cell. 2002;2(2):239-49.
1303 Epub 2002/02/08. doi: 10.1016/s1534-5807(02)00117-x. PubMed PMID: 11832249.
1304 44. Verstreken P, Ohyama T, Haueter C, Habets RL, Lin YQ, Swan LE, et al. Tweek, an
1305 evolutionarily conserved protein, is required for synaptic vesicle recycling. Neuron.
1306 2009;63(2):203-15. Epub 2009/07/31. doi: 10.1016/j.neuron.2009.06.017. PubMed PMID:
1307 19640479; PubMed Central PMCID: PMCPMC2759194.
1308 45. Wong R, Hadjiyanni I, Wei HC, Polevoy G, McBride R, Sem KP, et al. PIP2 hydrolysis and
1309 calcium release are required for cytokinesis in Drosophila spermatocytes. Curr Biol.
1310 2005;15(15):1401-6. Epub 2005/08/09. doi: 10.1016/j.cub.2005.06.060. PubMed PMID:
1311 16085493.

1312 46. West JJ, Zulueta-Coarasa T, Maier JA, Lee DM, Bruce AEE, Fernandez-Gonzalez R, et al. An
1313 Actomyosin-Arf-GEF Negative Feedback Loop for Tissue Elongation under Stress. Curr Biol.
1314 2017;27(15):2260-70 e5. Epub 2017/07/25. doi: 10.1016/j.cub.2017.06.038. PubMed PMID:
1315 28736167.
1316 47. Bhat HB, Ishitsuka R, Inaba T, Murate M, Abe M, Makino A, et al. Evaluation of
1317 aegerolysins as novel tools to detect and visualize ceramide phosphoethanolamine, a major
1318 sphingolipid in invertebrates. FASEB J. 2015;29(9):3920-34. Epub 2015/06/11. doi: 10.1096/fj.15-
1319 272112. PubMed PMID: 26060215.
1320 48. Dunst S, Kazimiers T, von Zadow F, Jambor H, Sagner A, Brankatschk B, et al. Endogenously
1321 tagged rab proteins: a resource to study membrane trafficking in Drosophila. Dev Cell.
1322 2015;33(3):351-65. Epub 2015/05/06. doi: 10.1016/j.devcel.2015.03.022. PubMed PMID:
1323 25942626; PubMed Central PMCID: PMCPMC4431667.
1324 49. Van Der Sluijs P, Hull M, Zahraoui A, Tavitian A, Goud B, Mellman I. The small GTP-binding
1325 protein rab4 is associated with early endosomes. Proc Natl Acad Sci U S A. 1991;88(14):6313-7.
1326 Epub 1991/07/15. doi: 10.1073/pnas.88.14.6313. PubMed PMID: 1906178; PubMed Central
1327 PMCID: PMCPMC52073.
1328 50. Pfeffer SR. Rab GTPases: specifying and deciphering organelle identity and function.
1329 Trends Cell Biol. 2001;11(12):487-91. Epub 2001/11/24. doi: 10.1016/s0962-8924(01)02147-x.
1330 PubMed PMID: 11719054.
1331 51. Albertson R, Riggs B, Sullivan W. Membrane traffic: a driving force in cytokinesis. Trends
1332 Cell Biol. 2005;15(2):92-101. Epub 2005/02/08. doi: 10.1016/j.tcb.2004.12.008. PubMed PMID:
1333 15695096.
1334 52. Echard A, Jollivet F, Martinez O, Lacapere JJ, Rousselet A, Janoueix-Lerosey I, et al.
1335 Interaction of a Golgi-associated kinesin-like protein with Rab6. Science. 1998;279(5350):580-5.
1336 Epub 1998/02/07. doi: 10.1126/science.279.5350.580. PubMed PMID: 9438855.
1337 53. Hegedus K, Takats S, Boda A, Jipa A, Nagy P, Varga K, et al. The Ccz1-Mon1-Rab7 module
1338 and Rab5 control distinct steps of autophagy. Mol Biol Cell. 2016;27(20):3132-42. Epub
1339 20160824. doi: 10.1091/mbc.E16-03-0205. PubMed PMID: 27559127; PubMed Central PMCID:
1340 PMCPMC5063620.
1341 54. Giansanti MG, Belloni G, Gatti M. Rab11 is required for membrane trafficking and
1342 actomyosin ring constriction in meiotic cytokinesis of Drosophila males. Mol Biol Cell.
1343 2007;18(12):5034-47. Epub 20071003. doi: 10.1091/mbc.e07-05-0415. PubMed PMID:
1344 17914057; PubMed Central PMCID: PMCPMC2096611.
1345 55. Polevoy G, Wei HC, Wong R, Szentpetery Z, Kim YJ, Goldbach P, et al. Dual roles for the
1346 Drosophila PI 4-kinase four wheel drive in localizing Rab11 during cytokinesis. J Cell Biol.
1347 2009;187(6):847-58. doi: 10.1083/jcb.200908107. PubMed PMID: 19995935; PubMed Central
1348 PMCID: PMCPMC2806325.
1349 56. Vanlandingham PA, Ceresa BP. Rab7 regulates late endocytic trafficking downstream of
1350 multivesicular body biogenesis and cargo sequestration. J Biol Chem. 2009;284(18):12110-24.
1351 Epub 20090305. doi: 10.1074/jbc.M809277200. PubMed PMID: 19265192; PubMed Central
1352 PMCID: PMCPMC2673280.
1353 57. Piper RC, Katzmann DJ. Biogenesis and function of multivesicular bodies. Annu Rev Cell
1354 Dev Biol. 2007;23:519-47. doi: 10.1146/annurev.cellbio.23.090506.123319. PubMed PMID:
1355 17506697; PubMed Central PMCID: PMCPMC2911632.

1356 58. Pollard TD. Nine unanswered questions about cytokinesis. J Cell Biol. 2017;216(10):3007-
1357 16. Epub 2017/08/16. doi: 10.1083/jcb.201612068. PubMed PMID: 28807993; PubMed Central
1358 PMCID: PMCPMC5626534.
1359 59. Ng MM, Chang F, Burgess DR. Movement of membrane domains and requirement of
1360 membrane signaling molecules for cytokinesis. Dev Cell. 2005;9(6):781-90. Epub 2005/12/06.
1361 doi: 10.1016/j.devcel.2005.11.002. PubMed PMID: 16326390.
1362 60. Rabionet M, van der Spoel AC, Chuang CC, von Tumpling-Radosta B, Litjens M,
1363 Bouwmeester D, et al. Male germ cells require polyenoic sphingolipids with complex
1364 glycosylation for completion of meiosis: a link to ceramide synthase-3. J Biol Chem.
1365 2008;283(19):13357-69. Epub 2008/03/01. doi: 10.1074/jbc.M800870200. PubMed PMID:
1366 18308723; PubMed Central PMCID: PMCPMC2442322.
1367 61. Wittmann A, Grimm MO, Scherthan H, Horsch M, Beckers J, Fuchs H, et al. Sphingomyelin
1368 Synthase 1 Is Essential for Male Fertility in Mice. PLoS One. 2016;11(10):e0164298. Epub
1369 2016/10/28. doi: 10.1371/journal.pone.0164298. PubMed PMID: 27788151; PubMed Central
1370 PMCID: PMCPMC5082796.
1371 62. Inaba T, Murate M, Tomishige N, Lee YF, Hullin-Matsuda F, Pollet B, et al. Formation of
1372 tubules and helical ribbons by ceramide phosphoethanolamine-containing membranes. Sci Rep.
1373 2019;9(1):5812. Epub 2019/04/11. doi: 10.1038/s41598-019-42247-1. PubMed PMID: 30967612;
1374 PubMed Central PMCID: PMCPMC6456502.
1375 63. Ghosh A, Kling T, Snaidero N, Sampaio JL, Shevchenko A, Gras H, et al. A global in vivo
1376 Drosophila RNAi screen identifies a key role of ceramide phosphoethanolamine for glial
1377 ensheathment of axons. PLoS Genet. 2013;9(12):e1003980. Epub 2013/12/19. doi:
1378 10.1371/journal.pgen.1003980. PubMed PMID: 24348263; PubMed Central PMCID:
1379 PMCPMC3861124.
1380 64. Schink KO, Tan KW, Stenmark H. Phosphoinositides in Control of Membrane Dynamics.
1381 Annu Rev Cell Dev Biol. 2016;32:143-71. Epub 2016/09/01. doi: 10.1146/annurev-cellbio-
1382 111315-125349. PubMed PMID: 27576122.
1383 65. Fremont S, Echard A. Membrane Traffic in the Late Steps of Cytokinesis. Curr Biol.
1384 2018;28(8):R458-R70. Epub 2018/04/25. doi: 10.1016/j.cub.2018.01.019. PubMed PMID:
1385 29689230.
1386 66. Abeytunga DT, Glick JJ, Gibson NJ, Oland LA, Somogyi A, Wysocki VH, et al. Presence of
1387 unsaturated sphingomyelins and changes in their composition during the life cycle of the moth
1388 Manduca sexta. J Lipid Res. 2004;45(7):1221-31. Epub 2004/04/23. doi: 10.1194/jlr.M300392-
1389 JLR200. PubMed PMID: 15102888.
1390 67. Fyrst H, Zhang X, Herr DR, Byun HS, Bittman R, Phan VH, et al. Identification and
1391 characterization by electrospray mass spectrometry of endogenous Drosophila sphingadienes. J
1392 Lipid Res. 2008;49(3):597-606. Epub 2007/12/25. doi: 10.1194/jlr.M700414-JLR200. PubMed
1393 PMID: 18156591.
1394 68. Kwon HC, Lee KC, Cho OR, Jung IY, Cho SY, Kim SY, et al. Sphingolipids from Bombycis
1395 Corpus 101A and their neurotrophic effects. J Nat Prod. 2003;66(4):466-9. Epub 2003/04/26. doi:
1396 10.1021/np0204491. PubMed PMID: 12713394.
1397 69. Basu J, Li Z. The Des-1 protein, required for central spindle assembly and cytokinesis, is
1398 associated with mitochondria along the meiotic spindle apparatus and with the contractile ring

1399 during male meiosis in Drosophila melanogaster. Mol Gen Genet. 1998;259(6):664-73. doi:
1400 10.1007/s004380050861. PubMed PMID: 9819060.
1401 70. Phan VH, Herr DR, Panton D, Fyrst H, Saba JD, Harris GL. Disruption of sphingolipid
1402 metabolism elicits apoptosis-associated reproductive defects in Drosophila. Dev Biol.
1403 2007;309(2):329-41. Epub 2007/08/21. doi: 10.1016/j.ydbio.2007.07.021. PubMed PMID:
1404 17706961; PubMed Central PMCID: PMCPMC2094363.
1405 71. Fyrst H, Oskouian B, Bandhuvula P, Gong Y, Byun HS, Bittman R, et al. Natural
1406 sphingadienes inhibit Akt-dependent signaling and prevent intestinal tumorigenesis. Cancer Res.
1407 2009;69(24):9457-64. Epub 2009/11/26. doi: 10.1158/0008-5472.CAN-09-2341. PubMed PMID:
1408 19934323; PubMed Central PMCID: PMCPMC2795098.
1409 72. Kumar A, Pandurangan AK, Lu F, Fyrst H, Zhang M, Byun HS, et al. Chemopreventive
1410 sphingadienes downregulate Wnt signaling via a PP2A/Akt/GSK3beta pathway in colon cancer.
1411 Carcinogenesis. 2012;33(9):1726-35. Epub 2012/05/15. doi: 10.1093/carcin/bgs174. PubMed
1412 PMID: 22581840; PubMed Central PMCID: PMCPMC3514901.
1413 73. Wiktorowska-Owczarek A, Berezinska M, Nowak JZ. PUFAs: Structures, Metabolism and
1414 Functions. Adv Clin Exp Med. 2015;24(6):931-41. Epub 2016/01/16. doi: 10.17219/acem/31243.
1415 PubMed PMID: 26771963.
1416 74. Feller SE, Gawrisch K. Properties of docosahexaenoic-acid-containing lipids and their
1417 influence on the function of rhodopsin. Curr Opin Struct Biol. 2005;15(4):416-22. Epub
1418 2005/07/26. doi: 10.1016/j.sbi.2005.07.002. PubMed PMID: 16039844.
1419 75. Rawicz W, Olbrich KC, McIntosh T, Needham D, Evans E. Effect of chain length and
1420 unsaturation on elasticity of lipid bilayers. Biophys J. 2000;79(1):328-39. Epub 2000/06/27. doi:
1421 10.1016/S0006-3495(00)76295-3. PubMed PMID: 10866959; PubMed Central PMCID:
1422 PMCPMC1300937.
1423 76. Endo K, Akiyama T, Kobayashi S, Okada M. Degenerative spermatocyte, a novel gene
1424 encoding a transmembrane protein required for the initiation of meiosis in Drosophila
1425 spermatogenesis. Mol Gen Genet. 1996;253(1-2):157-65. doi: 10.1007/s004380050308. PubMed
1426 PMID: 9003299.
1427 77. Palay SL, Palade GE. The fine structure of neurons. J Biophys Biochem Cytol. 1955;1(1):69-
1428 88. doi: 10.1083/jcb.1.1.69. PubMed PMID: 14381429; PubMed Central PMCID:
1429 PMCPMC2223597.
1430 78. Birks RI, Mackey MC, Weldon PR. Organelle formation from pinocytotic elements in
1431 neurites of cultured sympathetic ganglia. J Neurocytol. 1972;1(4):311-40. doi:
1432 10.1007/BF01102938. PubMed PMID: 8530968.
1433 79. Holtzman E, Peterson ER. Uptake of protein by mammalian neurons. J Cell Biol.
1434 1969;40(3):863-9. doi: 10.1083/jcb.40.3.863. PubMed PMID: 5765774; PubMed Central PMCID:
1435 PMCPMC2107638.
1436 80. Rosenbluth J, Wissig SL. The Distribution of Exogenous Ferritin in Toad Spinal Ganglia and
1437 the Mechanism of Its Uptake by Neurons. J Cell Biol. 1964;23:307-25. doi: 10.1083/jcb.23.2.307.
1438 PubMed PMID: 14222816; PubMed Central PMCID: PMCPMC2106519.
1439 81. Cooney JR, Hurlburt JL, Selig DK, Harris KM, Fiala JC. Endosomal compartments serve
1440 multiple hippocampal dendritic spines from a widespread rather than a local store of recycling
1441 membrane. J Neurosci. 2002;22(6):2215-24. PubMed PMID: 11896161; PubMed Central PMCID:
1442 PMCPMC6758269.

1443 82. Harding C, Heuser J, Stahl P. Receptor-mediated endocytosis of transferrin and recycling
1444 of the transferrin receptor in rat reticulocytes. J Cell Biol. 1983;97(2):329-39. doi:
1445 10.1083/jcb.97.2.329. PubMed PMID: 6309857; PubMed Central PMCID: PMCPMC2112509.
1446 83. Von Bartheld CS, Altick AL. Multivesicular bodies in neurons: distribution, protein content,
1447 and trafficking functions. Prog Neurobiol. 2011;93(3):313-40. Epub 20110107. doi:
1448 10.1016/j.pneurobio.2011.01.003. PubMed PMID: 21216273; PubMed Central PMCID:
1449 PMCPMC3055956.
1450 84. Weiner MP, Costa GL, Schoettlin W, Cline J, Mathur E, Bauer JC. Site-directed mutagenesis
1451 of double-stranded DNA by the polymerase chain reaction. Gene. 1994;151(1-2):119-23. Epub
1452 1994/12/30. doi: 10.1016/0378-1119(94)90641-6. PubMed PMID: 7828859.
1453 85. Bhat HB, Kishimoto T, Abe M, Makino A, Inaba T, Murate M, et al. Binding of a
1454 pleurotolysin ortholog from Pleurotus eryngii to sphingomyelin and cholesterol-rich membrane
1455 domains. J Lipid Res. 2013;54(10):2933-43. Epub 2013/08/07. doi: 10.1194/jlr.D041731. PubMed
1456 PMID: 23918047; PubMed Central PMCID: PMCPMC3770106.
1457 86. Baena V, Conrad R, Friday P, Fitzgerald E, Kim T, Bernbaum J, et al. FIB-SEM as a Volume
1458 Electron Microscopy Approach to Study Cellular Architectures in SARS-CoV-2 and Other Viral
1459 Infections: A Practical Primer for a Virologist. Viruses. 2021;13(4). Epub 20210402. doi:
1460 10.3390/v13040611. PubMed PMID: 33918371; PubMed Central PMCID: PMCPMC8066521.
1461 87. Paul-Gilloteaux P, Heiligenstein X, Belle M, Domart MC, Larijani B, Collinson L, et al. eC-
1462 CLEM: flexible multidimensional registration software for correlative microscopies. Nat Methods.
1463 2017;14(2):102-3. doi: 10.1038/nmeth.4170. PubMed PMID: 28139674.
1464 88. Fyrst H, Herr DR, Harris GL, Saba JD. Characterization of free endogenous C14 and C16
1465 sphingoid bases from Drosophila melanogaster. J Lipid Res. 2004;45(1):54-62. Epub 2003/09/18.
1466 doi: 10.1194/jlr.M300005-JLR200. PubMed PMID: 13130120.
1467 89. Merrill AH, Jr., Sullards MC, Allegood JC, Kelly S, Wang E. Sphingolipidomics: high-
1468 throughput, structure-specific, and quantitative analysis of sphingolipids by liquid
1469 chromatography tandem mass spectrometry. Methods. 2005;36(2):207-24. Epub 2005/05/17.
1470 doi: 10.1016/j.ymeth.2005.01.009. PubMed PMID: 15894491.
1471

1472

1473

1474

1475

1476

1477

1478

1479

1480 **Supplemental movie legends**

1481 **Movie S1.** Live cell imaging of neuroblast asymmetric divisions in 3rd instar larval brain. GFP
1482 tagged PH domain of PIP3 binding protein Step was expressed under the control of alpha
1483 tubulin84B promoter. Arrows indicate enrichment of GFP-Step on cleavage furrow membranes
1484 during cytokinesis.
1485

1486 **Movie S2.** Live cell imaging of an intact control *Drosophila* spermatocyte cyst undergoing
1487 meiosis I cytokinesis. Spermatocytes are expressing myosin II regulatory light chain (RLC)
1488 tagged to GFP under its own promoter and Ubi-p63E promotor drives the expression of Feo-
1489 mCherry. An intact cyst is shown. Sqh-GFP-RLC localizes to actomyosin contractile ring. Feo-
1490 mCherry localizes to central spindle.
1491
1492 **Movie S3.** Live cell imaging of an intact *cpes* mutant spermatocyte cyst undergoing meiosis I
1493 cytokinesis. Mutant spermatocytes are expressing myosin II regulatory light chain (RLC) tagged
1494 to GFP under its own promoter and Feo-mCherry was expressed under the control of Ubi-p63E
1495 promotor. Sqh-GFP-RLC specifically localizes to actomyosin contractile ring. Feo-mCherry
1496 localizes to central spindle.
1497
1498 **Movie S4.** Live cell imaging of an intact CPES rescue spermatocyte cyst undergoing meiosis I
1499 cytokinesis. The UAS-CPES is expressed using Tub-Gal4. Spermatocytes are also expressing
1500 Sqh-GFP-RLC and Feo-mCherry. Sqh-GFP-RLC specifically localizes to actomyosin contractile
1501 ring. Feo-mCherry localizes to central spindle.
1502
1503 **Movie S5.** Live cell imaging of an intact control *Drosophila* spermatocyte cyst undergoing
1504 meiosis I cytokinesis. The UAS PLCδ-PH-EGFP is expressed using Tub-Gal4 and Feo-mCherry
1505 is expressed under the control of Ubi-p63E promoter. PLCδ-PH-EGFP specifically binds to PIP2
1506 at the plasma membrane. Feo-mCherry localizes to central spindle.
1507
1508 **Movie S6.** Live cell imaging of an intact *cpes* mutant spermatocyte cyst undergoing meiosis I
1509 cytokinesis. Tub-Gal4 drives the expression of UAS PLCδ-PH-EGFP and Ubi-p63E promoter
1510 drives the expression of Feo-mCherry. PLCδ-PH-EGFP specifically binds to PIP2 at the plasma
1511 membrane. Feo-mCherry localizes to central spindle.
1512
1513 **Movie S7.** Live cell imaging of an intact CPES rescue spermatocyte cyst undergoing meiosis I
1514 cytokinesis. The UAS-CPES and UAS PLCδ-PH-EGFP are expressed using Tub-Gal4. The Feo-
1515 mCherry is expressed under the control of Ubi-p63E promoter. PLCδ-PH-EGFP specifically
1516 binds to PIP2 at the plasma membrane. Feo-mCherry localizes to central spindle.
1517
1518 **Movie S8.** Live cell imaging of an intact control *Drosophila* spermatocyte cyst undergoing
1519 meiosis I cytokinesis. Alpha tubulin84B promoter drives the expression of GFP tagged PH
1520 domain of Step that specifically binds to PIP3 at the plasma membrane. Feo-mCherry localizes
1521 to central spindle.
1522

1523 **Movie S9.** Live cell imaging of an intact *cpes* mutant spermatocyte cyst undergoing meiosis I
1524 cytokinesis. The GFP-tagged PH domain of Step is expressed under the control of alpha
1525 tubulin84B promoter and Feo-mCherry is expressed under the control of Ubi-p63E promoter.
1526 The GFP-PH-Step specifically localizes to PIP3 at the plasma membrane and Feo-mCherry
1527 localizes to central spindle.
1528
1529 **Movie S10.** Live cell imaging of an intact CPES rescue spermatocyte cyst undergoing meiosis I
1530 cytokinesis. PH domain of Step is tagged to GFP and expressed under the control of alpha
1531 tubulin84B promoter and Feo-mCherry is expressed under the control of Ubi-p63E promoter.
1532 The UAS-CPES expression is driven by Tub-Gal4. The GFP-PH-Step specifically localizes to
1533 PIP3 at the plasma membrane and Feo-mCherry localizes to central spindle.
1534
1535 **Movie S11.** Live cell imaging of EYFP-Rab7 expressing spermatocytes treated with recombinant
1536 CPE binding protein tagged to mCherry (PlyA2-mCherry). The EYFP-Rab7 is expressed under
1537 its own promotor.
1538
1539 **Movie S12.** Live cell imaging of EYFP-Rab11 expressing spermatocytes treated with
1540 recombinant PlyA2-mCherry. EYFP-Rab11 is expressed under its own promotor.
1541
1542 **Movie S13.** Live cell imaging of *rab7* mutant spermatocytes treated with recombinant CPE
1543 binding protein tagged to mCherry (PlyA2-mCherry).
1544
1545 **Movie S14.** FIB-SEM image stack corresponding to "Figure 7B"
1546
1547 **Movie S15.** Live cell imaging of control *Drosophila* spermatocyte cyst undergoing meiosis I
1548 cytokinesis. The EYFP-Rab7 is expressed under its own promotor. Tubulin Gal4 drives the
1549 expression mRFP-Anillin that localizes to contractile ring.
1550
1551 **Movie S16.** Movie showing the FIB-SEM volume reconstruction of the dividing cells in "Figure
1552 1K", highlighting the points at which vesicle docking at the furrow could be captured. Cells were
1553 3D rendered in grayscale and overlaid by manually segmented 3D models of the cleavage furrow
1554 (red), undocked vesicles (green) and docked vesicles (blue).
1555
1556 **Movie S17.** Movie showing the FIB-SEM sub-volume reconstruction of the dividing cells in
1557 "Figure 8N", highlighting the points at which vesicle docking at the furrow could be captured.
1558
1559 **Movie S18.** Live cell imaging of cpes mutant spermatocytes expressing EYFP-Rab7 under its
1560 own promotor and mRFP-Anillin driven by tubulin-Gal4.
1561

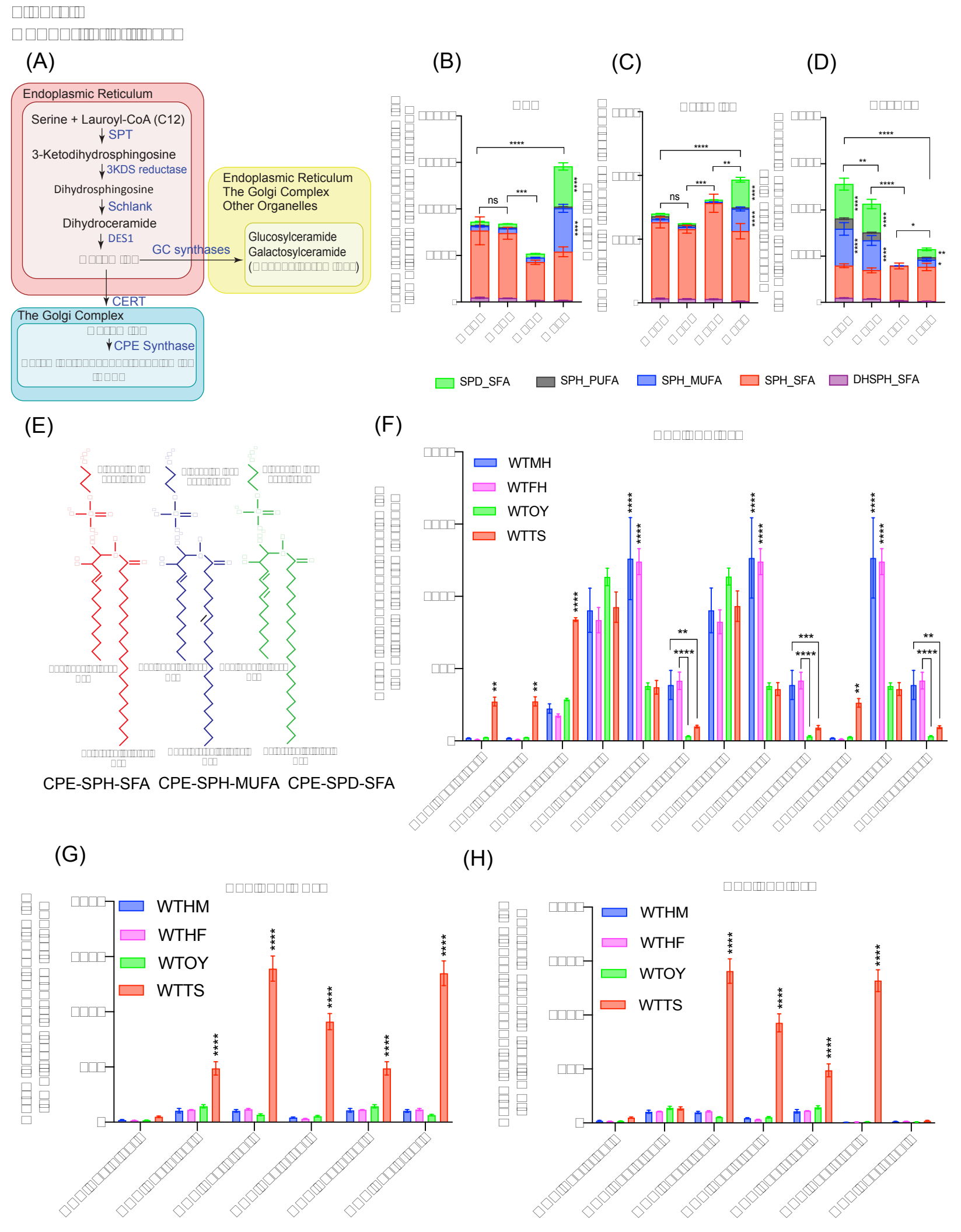
(A)
Endoplasmic Reticulum
Serine + Lauroyl-CoA (C12)
SPT
3-Ketodihydrosphingosine
3KDS reductase
Dihydrosphingosine
Schlank
Dihydroceramide
DES1
GC synthases
CERT
The Golgi Complex
CPE Synthase
Endoplasmic Reticulum
The Golgi Complex
Other Organelles
Glucosylceramide
Galactosylceramide
(B)
(C)
(D)
ns
SPD_SFA
SPH_PUFA
SPH_MUFA
SPH_SFA
DHSPH_SFA
(E)
CPE-SPH-SFA
CPE-SPH-MUFA
CPE-SPD-SFA
(F)
WTMH
WTFH
WTOY
WTTS
(G)
WTHM
WTHF
WTOY
WTTS
(H)
WTHM
WTHF
WTOY
WTTS

Figure 2
Kunduri et al., 2022

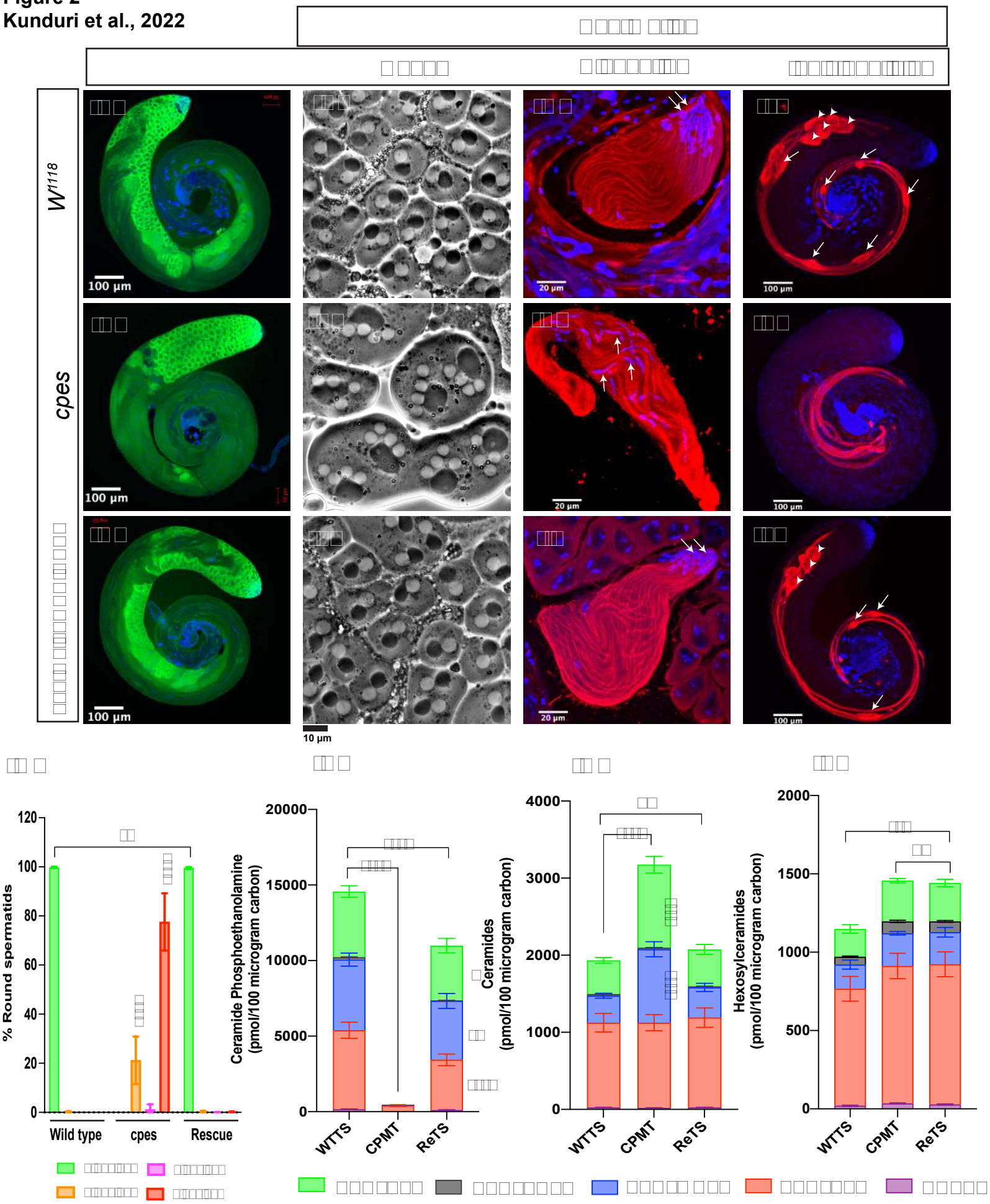

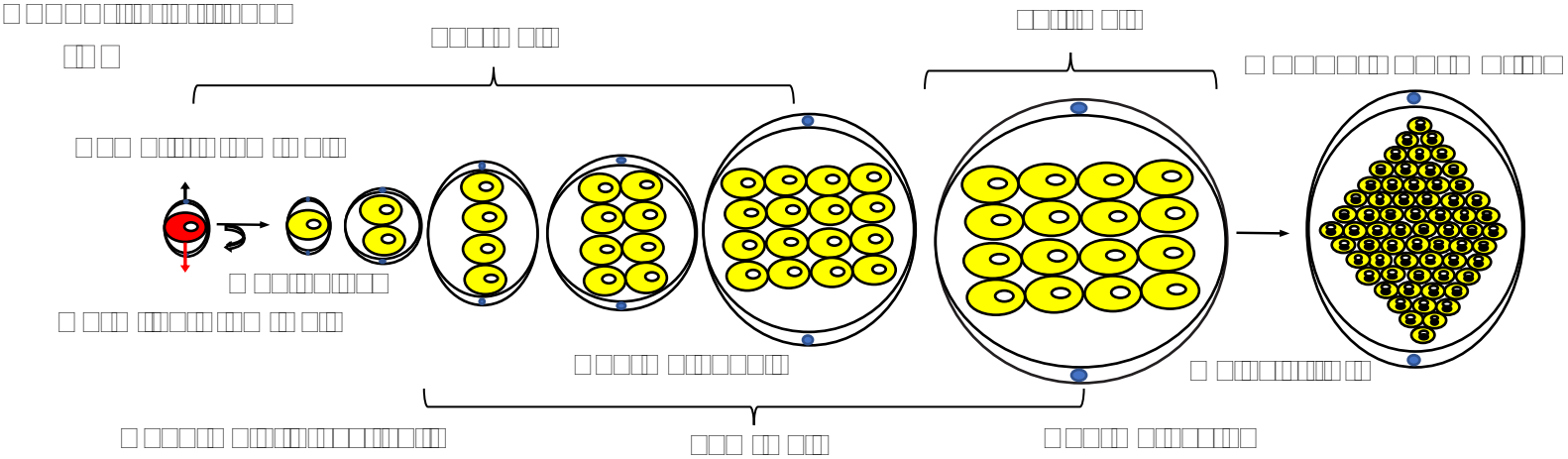

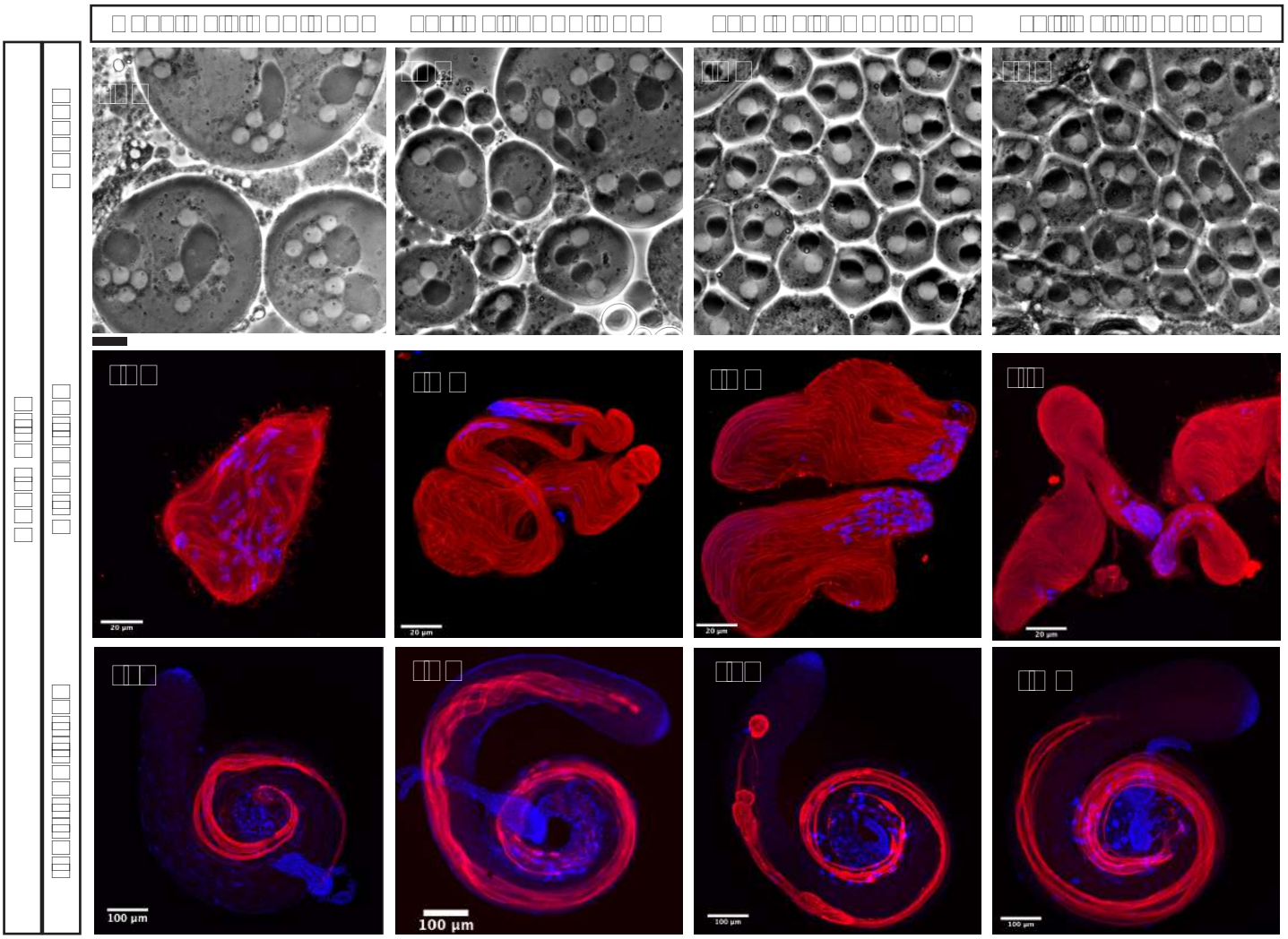
100 µm
100 µm

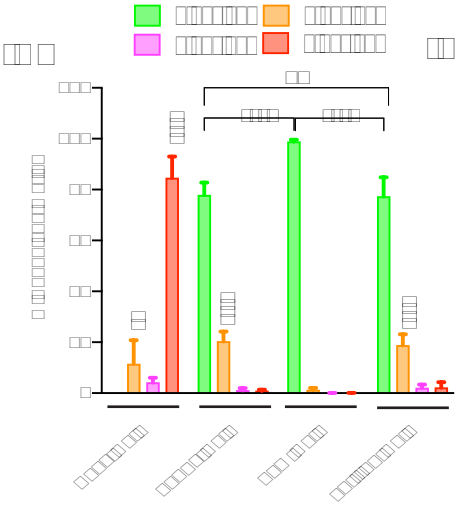

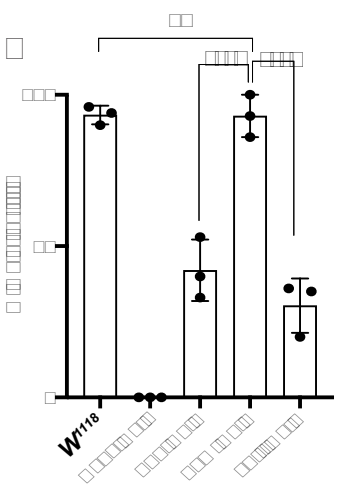
W1118

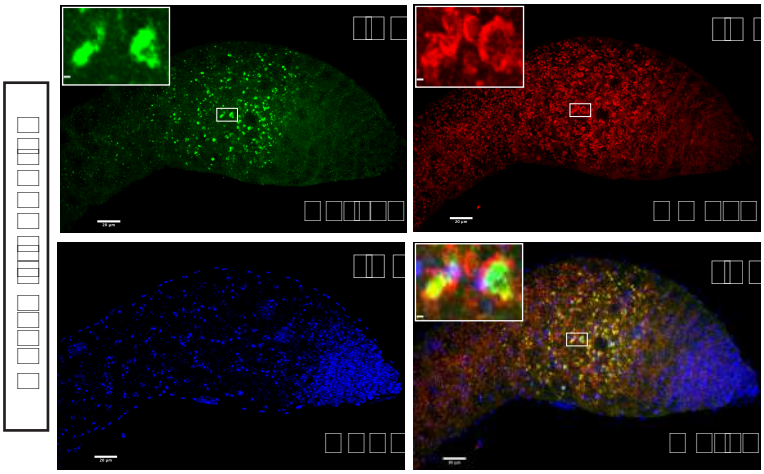

Figure 4
Kunduri et al., 2022

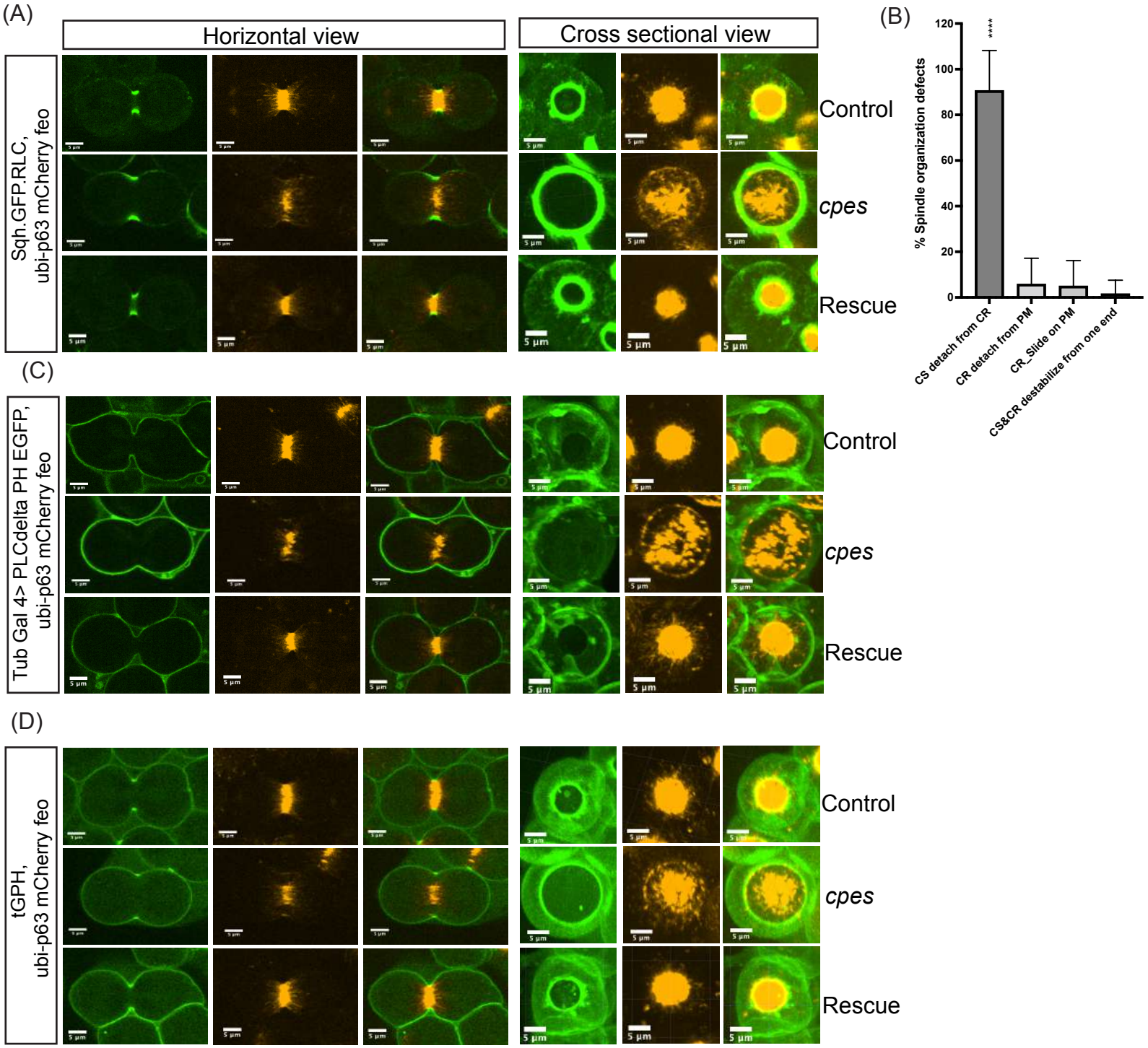

Figure 5
Kunduri et al., 2022

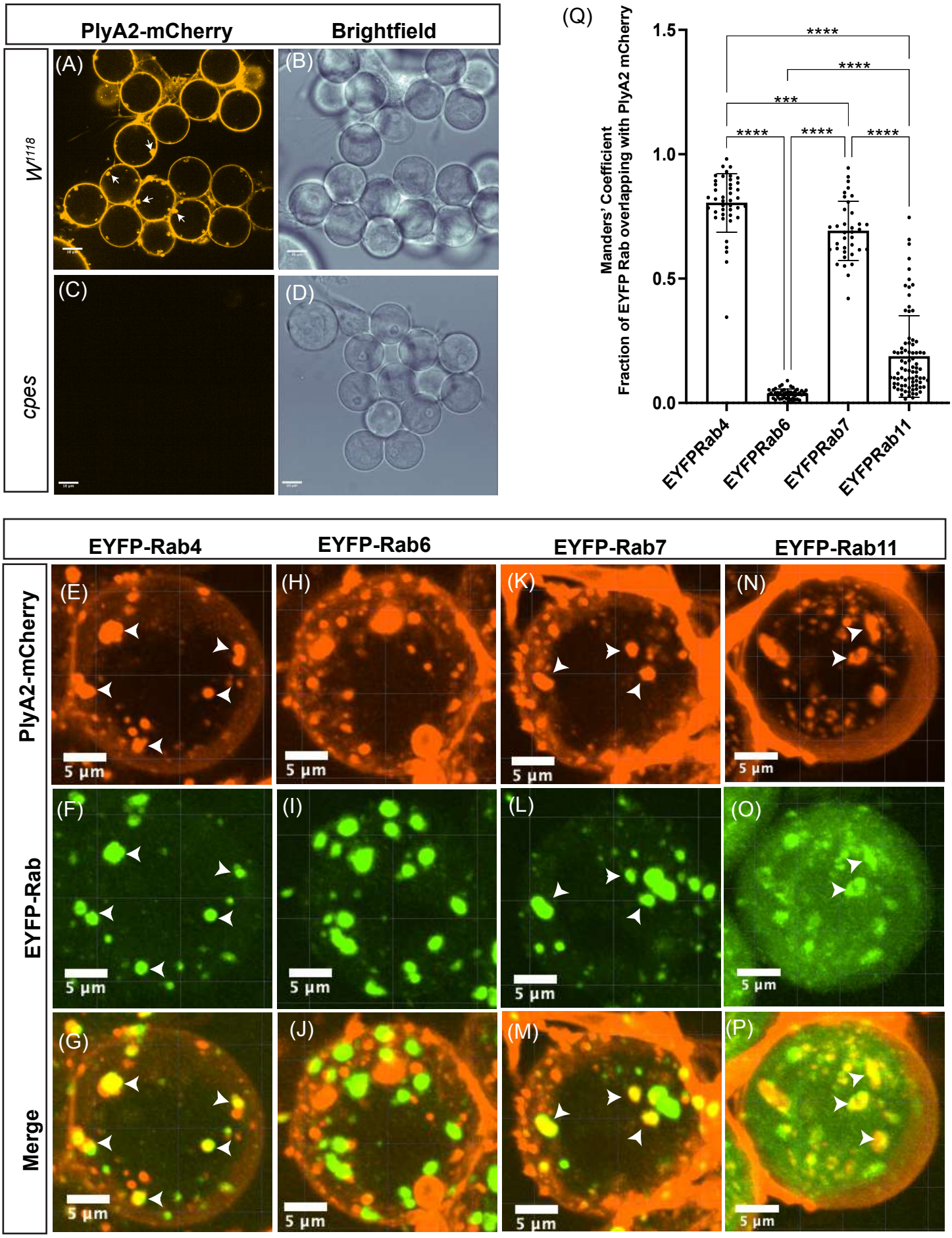

Figure 6
Kunduri et al., 2022

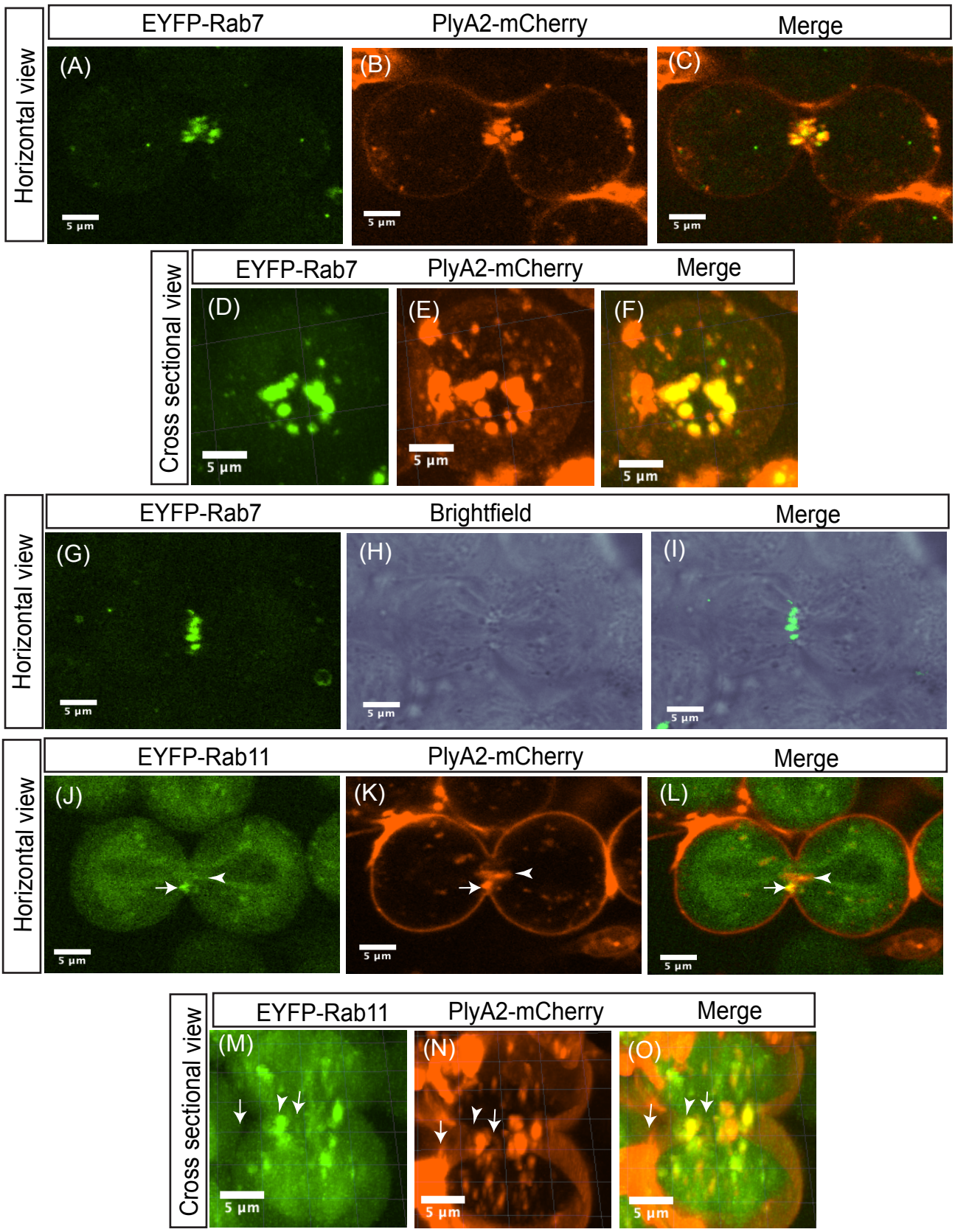

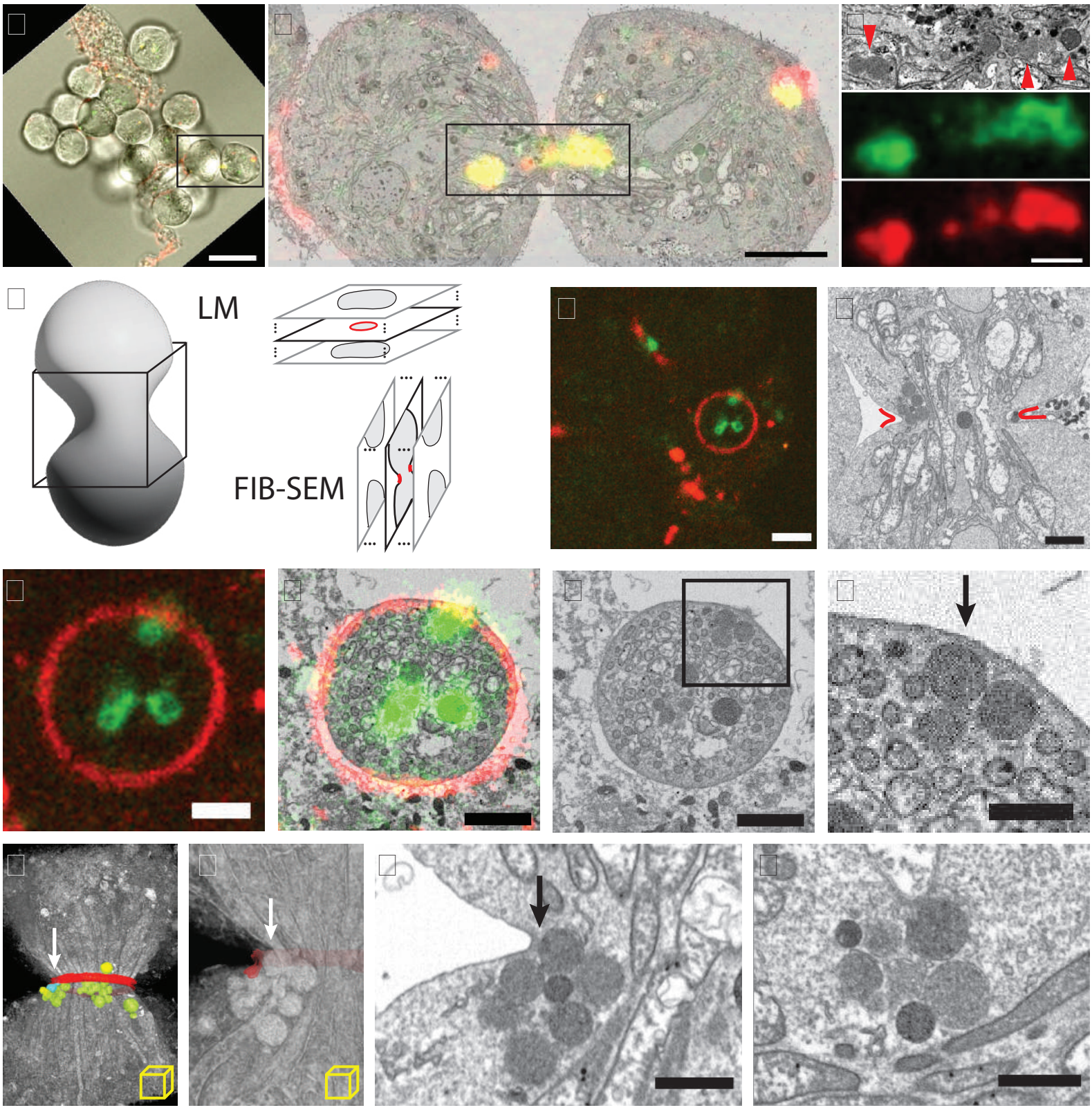
LM
FIB-SEM

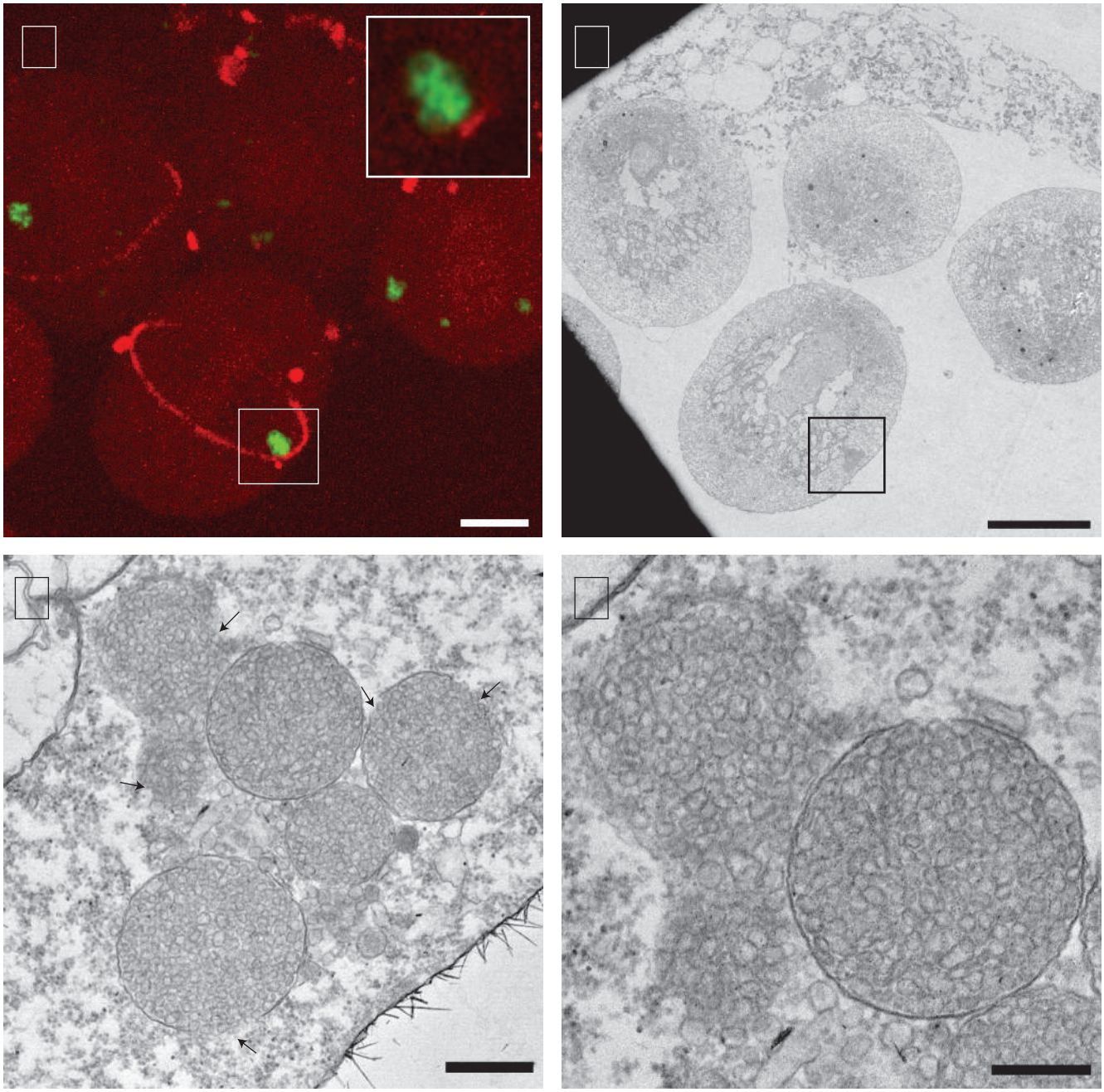

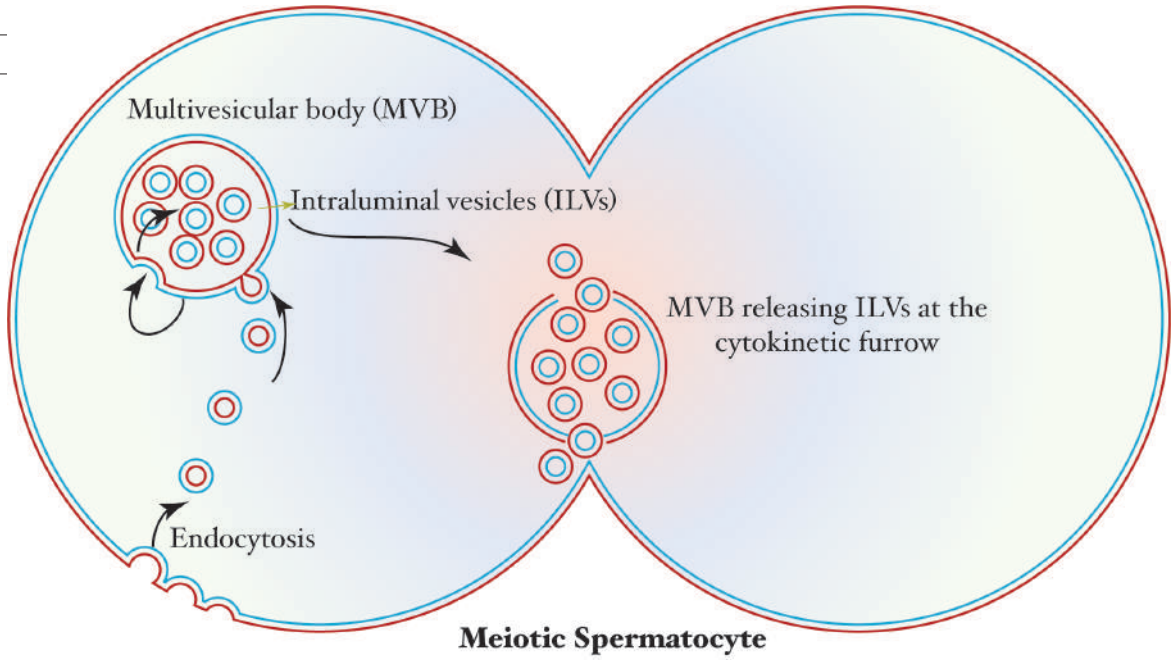
Multivesicular body (MVB)
Intraluminal vesicles (ILVs)
MVB releasing ILVs at the cytokinetic furrow
Endocytosis
Meiotic Spermatocyte